Scientific paper

Multiscale Model for Creep of Shotcrete - From Logarithmic-Type Viscous Behavior of CSH at the μm-Scale to Macroscopic Tunnel Analysis

Christian Pichler[1], Roman Lackner[2] and Herbert A. Mang[3]

Received 10 July 2007, accepted 18 October 2007

Abstract

A previously published multiscale model for early-age cement-based materials [Pichler *et al*. 2007. "A multiscale micromechanics model for the autogenous-shrinkage deformation of early-age cement-based materials." *Engineering Fracture Mechanics*, 74, 34-58] is extended towards upscaling of viscoelastic properties. The obtained model links macroscopic behavior, i.e., creep compliance of concrete samples, to the composition of concrete at finer scales and the (supposedly) intrinsic material properties of distinct phases at these scales. Whereas finer-scale composition (and its history) is accessible through recently developed hydration models for the main clinker phases in ordinary Portland cement (OPC), viscous properties of the creep active constituent at finer scales, i.e., calcium-silicate-hydrates (CSH) are identified from macroscopic creep tests using the proposed multiscale model. The proposed multiscale model is assessed by different concrete creep tests reported in the open literature. Moreover, the model prediction is compared to empirical creep models, such as the so-called B3 model. Finally, the developed multiscale model is incorporated in the macroscopic analysis of shotcrete tunnel linings. Hereby, the early-age properties of shotcrete are specified by the presented multiscale model, taking mix design, cement characteristics, and on-site conditions into account.

1. Origin of creep of cement-based materials

Modeling of creep of cement-based materials and the identification of the underlying physical processes in the calcium-silicate-hydrates (CSH)[*1] at finer observation scales remain intensively discussed topics within the scientific community. Bažant and coworkers (see, e.g., Bažant *et al*. (1997)) have developed the, to date, most widely used model for creep of early-age cement-based materials. According to Bažant *et al*. (1997), the source of creep is the relaxation of *microprestress*, which is generated as a reaction to the disjoining pressure in micropores (intra-hydrate pores). Increased stresses at these so-called creep sites increase the ease of bond breakage and, hence, increase the creep rate. Hereby, recently formed hydration products contain a high density of creep sites, whereas continuous microprestress relaxation reduces the creep potential of CSH.

Recently, Jennings pointed out that "*... there are fundamental chemical and thermodynamic arguments against the idea that large internal stresses are formed during hydration. CSH forms under near-equilibrium conditions with respect to the aqueous phase, making it unlikely that high internal stresses that could act as creep sites would develop ...*" (Thomas and Jennings 2006). Jennings and coworkers have developed a structural model for CSH at the nanometer-scale accounting for the colloidal nature of CSH. Hereby, CSH is described as an aggregation of precipitated, colloid-sized particles (Jennings 2000, 2004) with the "basic building blocks" (radius of 1.1 nm) aggregating into "spherical globules" (radius of 2.8 nm). The latter aggregate further into (i) low-density CSH (CSH-LD) or (ii) high-density CSH (CSH-HD), depending on *w*/*c*-ratio, age, and environmental conditions (Jennings 2000, 2004). According to Jennings (2004), the origin of viscous deformations is explained by the re-arrangement (dislocation) of globules under shear stress (or drying).

In both microscopic (Pichler and Lackner 2007) and macroscopic creep tests, a logarithmic-type behavior is encountered, i.e., the creep compliance is proportional to $\ln(1 + t/\tau^{v})$, where τ^{v} denotes the characteristic time of the creep process. According to Nabarro (2001), the two mechanisms leading to logarithmic creep in crystalline solids are either

- *work hardening*: dislocations move forward under the applied stress by overcoming potential barriers, while successively raising the height of the potential barriers or
- *exhaustion*: while neglecting work hardening, the barriers to dislocation motion do not have equal activation energies; those with relatively small activation energies are overcome faster than those with

[1]University Assistant, Institute for Mechanics of Materials and Structures, Vienna University of Technology, Austria.
E-mail: Christian.Pichler@tuwien.ac.at
[2]Professor, FG Computational Mechanics, Technical University of Munich, Germany.
[3]Professor, Institute for Mechanics of Materials and Structures, Vienna University of Technology, Austria.

[*1] Standard cement chemistry abbreviations are used throughout this paper: C=CaO, S=SiO_2, A=Al_2O3, F=Fe_2O_3, S=SO_3, H=H_20.

relatively large activation energies; if each barrier which is overcome contributes an equal increment of strain, the total strain increases linearly with the increasing activation energy, where the latter is a logarithmic function of time.

The mentioned dislocation-based mechanism is consistent with the creep mechanism proposed in Jennings (2004).

In this paper, the logarithmic-type creep behavior encountered during nanoindentation tests is transferred to the macroscale by developing a multiscale model for basic creep of early-age cement-based materials. With the multiscale model at hand, viscous properties of the creep-active constituent at finer scales, i.e., CSH, can be assessed by means of results from macroscopic creep tests. The focus of this paper is on the experimental identification of CSH creep properties suitable for multiscale modeling, avoiding speculative arguments on the physical/chemical processes associated with creep. Microstructural changes associated with creep such as, e.g., bond breakage take place at a far finer scale as investigated by nanoindentation. Thus, the employed constitutive law for CSH (μm-scale) represent these processes (nm-scale) in a homogenized manner.

The paper is structured as follows: In Sections 2 and 3 the previously developed multiscale model (Pichler *et al*. 2007) and upscaling of elastic properties are reviewed. Section 4 deals with upscaling of the viscoelastic compliance. The presented upscaling scheme is used in Section 5 for determination of creep parameters of CSH through a top-down application of the multiscale model starting from macroscopic creep tests. Finally, the multiscale model is employed for determination of early-age properties of shotcrete in the context of a hybrid analysis of shotcrete tunnel linings (Section 6).

2. Proposed multiscale model

The multiscale model proposed in Pichler *et al*. (2007) for upscaling of viscoelastic properties and autogenous-shrinkage of early-age cement-based materials comprises four length scales, which are identified as (see **Fig. 1**)[*2]:

- Scale I comprises the four clinker phases, high-density CSH (CSH-HD) and low-density CSH (CSH-LD), and the water and air phase. The four clinker phases, which do not exhibit time-dependent behavior, are condensed into one material phase (Scale Ia). The constituents showing time-dependent behavior, on the other hand, are combined at Scale Ib-1, where CSH-HD is located in the space confined by the previously formed CSH-LD. At the porous CSH scale (Scale Ib-2), water and air are considered as inclusions in a matrix constituted by the homogenized material of Scale Ib-1.
- At Scale II (*cement-paste scale*), anhydrous cement (homogenized material of Scale Ia), gypsum $C\bar{S}H_2$, portlandite CH, and reaction products from C_3A and C_4AF hydration form inclusions in a matrix constituted by the homogenized material of Scale Ib-2.
- At Scale III (*mortar or concrete scale*), aggregates are represented as inclusions in the cement paste (homogenized material of Scale II). In addition to aggregates and cement paste, the interface transition zone (ITZ) may be introduced at Scale II. Since the ITZ mainly influences strength and transport properties of concrete rather than viscous deformations, it is not considered in the present model.
- Finally, at Scale IV (*macroscale*), concrete is treated as a continuum.

In order to determine the volume fractions of the different phases in the respective RVEs, the following set of stoichiometric reactions is employed for the four main clinker phases of ordinary Portland cement (OPC) (Tennis and Jennings 2000):

$$C_3S + 5.3H \rightarrow 0.5C_{3.4}S_2H_8 + 1.3CH \quad (1)$$

$$C_2S + 4.3H \rightarrow 0.5C_{3.4}S_2H_8 + 0.3CH \quad (2)$$

$$C_4AF + 2CH + 10H \rightarrow 2C_3(A,F)H_6 \quad (3)$$

$$C_3A + 3C\bar{S}H_2 + 26H \rightarrow C_6A\bar{S}_3H_{32} \quad (4)$$

$$C_3A + 0.5C_6A\bar{S}_3H_{32} + 2H \rightarrow 1.5C_4A\bar{S}H_{12} \quad (5)$$

$$C_3A + CH + 12H \rightarrow C_4AH_{13} \quad (6)$$

Eqs. (4) to (6) describe the formation of calcium alumi-

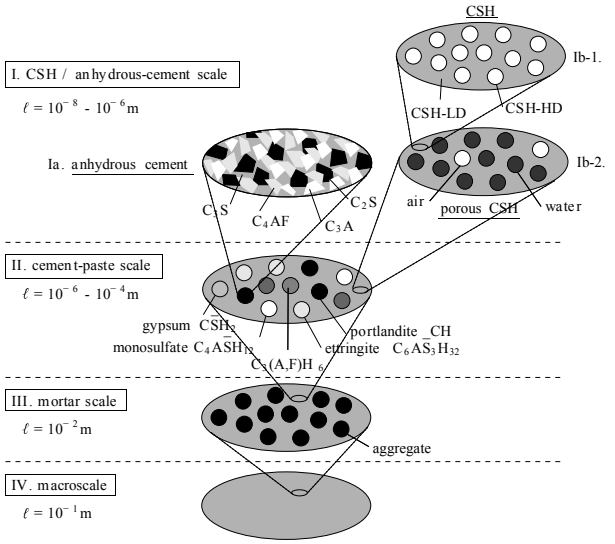

Fig. 1 Scales of observation for upscaling of properties of cement-based materials [ℓ = size of representative volume element (RVE)].

[*2]Morphological investigations at lower scales of observation can be found in, e.g., Bentz (1997) [anhydrous cement], Diamond (2004) [cement paste], and Neubauer and Jennings (2000) [CSH].

nate hydrates from C_3A in the presence of gypsum, which is added to prevent rapid setting of C_3A.

The hydration extent is described by the degree of hydration of the clinker phases, ξ_x with $x \in \{C_3S, C_2S, C_4AF\}$. A recently developed (Bernard *et al.* 2003) and refined (Pichler 2007) kinetics model is used to determine the hydration history $\xi_x(t)$. Input parameters for the kinetics model comprise the Blaine (grinding) fineness ø of the employed Portland cement, the medium initial radius of the clinker grains R, the mass fractions of the clinker phases, and the water/cement-ratio w/c. Based on the stoichiometric reactions given in Eqs. (1) to (6), and the molar masses M and densities ρ of the different material phases (see, e.g., Tennis and Jennings (2000)), the volume fractions of the different phases (at the cement-paste scale) can be determined as a function of the hydration degrees ξ_x and the mass fractions of the clinker phases m_x. This is shown exemplarily for the volume fraction of $C_{3.4}S_2H_8$ appearing in Eqs. (1) and (2):

$$f_{C_{3.4}S_2H_8}(t) = \left[\xi_{C_3S}(t) \frac{m_{C_3S}}{M_{C_3S}} \frac{0.5 M_{C_{3.4}S_2H_8}}{\rho_{C_{3.4}S_2H_8}} + \xi_{C_2S}(t) \frac{m_{C_2S}}{M_{C_2S}} \frac{0.5 M_{C_{3.4}S_2H_8}}{\rho_{C_{3.4}S_2H_8}} \right] \bar{\rho} \tag{7}$$

with

$$\bar{\rho} = \frac{1}{\sum_x \frac{m_x}{\rho_x} + \frac{w/c}{\rho_H} \sum_x m_x} \tag{8}$$

The overall degree of hydration, ξ, is computed as

$$\xi = \frac{\sum_x m_x \xi_x}{\sum_x m_x} \tag{9}$$

where $x \in \{C_3S, C_2S, C_3A, C_4AF, C\bar{S}H_2\}$ and m_x representing the mass fractions of the four clinker phases and gypsum. Hereby, $\xi_{C\bar{S}H_2}$ is linearly coupled to ξ_{C_3A} [see Eq. (4)]. **Figure 2** shows the evolution of the volume fractions at the cement-paste scale as a function of ξ for shotcrete with a w/c of 0.48 (see **Appendix 2(a)**).

3. Upscaling of elastic properties

The four length scales introduced in the previous section obey the separability of scale condition, i.e., they are separated one from each other by at least one order of magnitude. With volume fractions of the different phases at the respective observation scales at hand, continuum micromechanics is employed to estimate effective elastic properties. For homogenization at Scale Ia, the self-consistent (SC) scheme, suitable for a polycrystalline microstructure, is used (Kroener 1958; Hershey 1954). During homogenization at Scales Ib to III, the

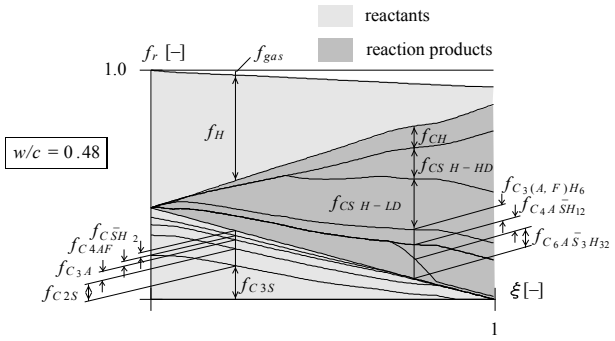

Fig. 2 Variation of the volume fractions at the cement-paste scale as a function of the overall degree of hydration ξ for shotcrete employed at the Lainzer tunnel (see Appendix 2(a)).

matrix-inclusion type morphology is taken into account by the Mori-Tanaka scheme (MT) (Mori and Tanaka 1973). Homogenization schemes based on continuum micromechanics consider a representative volume element (RVE) subjected to a homogeneous strain $\mathbf{E}$ at its boundary. These schemes depart from the definition of the so-called strain-localization tensor $\mathbb{A}$ linking the effective strain tensor $\mathbf{E}$ with the local strain tensor $\boldsymbol{\varepsilon}$ at the location $\mathbf{x}$:

$$\boldsymbol{\varepsilon}(\mathbf{x}) = \mathbb{A}(\mathbf{x}) : \mathbf{E} \tag{10}$$

The effective strain tensor $\mathbf{E}$ represents the volume average of the local strain tensor ε:

$$\mathbf{E} = \langle \varepsilon(\mathbf{x}) \rangle_V = \frac{1}{V} \int_V \varepsilon(\mathbf{x}) dV \tag{11}$$

Inserting Eq. (10) into Eq. (11), one gets $\mathbf{E} = \langle \mathbb{A}(\mathbf{x}) \rangle_V : \mathbf{E}$ and, thus, $\langle \mathbb{A}(\mathbf{x}) \rangle_V = \mathbb{I}$. Considering an ellip-soidal inclusion i embedded in a reference medium characterized by the material tensor $\mathbb{c}_0$, the strain-localization tensor $\mathbb{A}$ within the domain i is constant and given by (Eshelby 1957)

$$\mathbb{A}_i = \left[\mathbb{I} + \mathbb{S}_i : (\mathbb{c}_0^{-1} : \mathbb{c}_i - \mathbb{I}) \right]^{-1} : \left\{ \sum_{r=0,i} f_r \left[\mathbb{I} + \mathbb{S}_r : (\mathbb{c}_0^{-1} : \mathbb{c}_r - \mathbb{I}) \right]^{-1} \right\}^{-1} = \text{const} \tag{12}$$

with $\mathbb{c}_i$ as the material tensor of the inclusion i and $\mathbb{c}_0$ as the material tensor of the reference medium. $\mathbb{S}_i$ denotes the Eshelby tensor, conditioned by the geometric properties of the inclusion and the elastic properties of the reference medium.

The volume average of the local stress tensor $\boldsymbol{\sigma}(\mathbf{x})$ determines the effective stress tensor $\boldsymbol{\Sigma}$:

$$\boldsymbol{\Sigma} = \langle \boldsymbol{\sigma}(\mathbf{x}) \rangle_V = \frac{1}{V} \int_{\mathcal{V}} \boldsymbol{\sigma}(\mathbf{x}) dV \tag{13}$$

Considering a linear-elastic constitutive law for the r-th material phase, linking the local strain tensor with the local stress tensor,

$$\boldsymbol{\sigma}_r(\mathbf{x}) = \mathbb{c}_r : \boldsymbol{\varepsilon}_r(\mathbf{x}) \tag{14}$$

and Eq. (10) in Eq. (13) one gets

$$\boldsymbol{\Sigma} = \left\langle \mathbb{c}(\mathbf{x}) : \mathbb{A}(\mathbf{x}) \right\rangle_V : \mathbf{E} \tag{15}$$

Comparison with $\boldsymbol{\Sigma} = \mathbb{C}_{eff} : \mathbf{E}$[*3] gives access to the effective material tensor $\mathbb{C}_{eff}$:

$$\mathbb{C}_{eff} = \left\langle \mathbb{c}(\mathbf{x}) : \mathbb{A}(\mathbf{x}) \right\rangle_V \tag{16}$$

Considering the morphology of the composite material, the unknown strain localization tensor $\mathbb{A}$, which so far is available for a single inclusion [Eq. (12)], can be estimated based on the choice of $\mathbb{c}_0$:

- In case the microstructure is characterized by a distinct matrix/inclusion-type morphology, $\mathbb{c}_0$ is set equal to the material tensor of the matrix material $\mathbb{c}_m$. This estimation leads to the Mori-Tanaka (MT) scheme (Mori and Tanaka 1973).
- For a polycrystalline microstructure, i.e., the material phases are equally dispersed, and none of them forms a matrix, $\mathbb{c}_0$ is replaced by the effective material tensor $\mathbb{C}_{eff}$. The obtained implicit method is referred to as self-consistent (SC) scheme (Hershey 1954; Kroener 1958).

Using

$$\begin{aligned} \left\langle \mathbb{A}(\mathbf{x}) \right\rangle_V &= \frac{V_0}{V} \left\langle \mathbb{A}(\mathbf{x}) \right\rangle_{V_0} + \frac{V_i}{V} \left\langle \mathbb{A}(\mathbf{x}) \right\rangle_{V_i} = \mathbb{I} \\ &\rightarrow f_0 \left\langle \mathbb{A}(\mathbf{x}) \right\rangle_{V_0} = \mathbb{I} - f_i \mathbb{A}_i \end{aligned} \tag{17}$$

where $\left\langle \mathbb{A}(\mathbf{x}) \right\rangle_{V_i} = \mathbb{A}_i$ = const. was used and f_i and f_0 denote the volume fractions of the inclusion and reference medium, respectively, and Eq. (12), one gets the volume average of the localization tensor over the reference medium as[*4]

$$\left\langle \mathbb{A}(\mathbf{x}) \right\rangle_{V_0} = \left\{ \sum_{r \in 0,i} f_r [\mathbb{I} + \mathbb{S}_r : (\mathbb{c}_0^{-1} : \mathbb{c}_r - \mathbb{I})]^{-1} \right\}^{-1} \tag{19}$$

Considering Eqs. (19) and (12) in Eq. (16) gives access to the effective material tensor

$$\begin{aligned} \mathbb{C}_{eff} &= f_0 \mathbb{c}_0 : \left\langle \mathbb{A}(\mathbf{x}) \right\rangle_{V_0} + f_i \mathbb{c}_i : \mathbb{A}_i \\ &= \left\{ \sum_{r \in 0,i} f_r \mathbb{c}_r : \left[\mathbb{I} + \mathbb{S}_r : \left(\mathbb{c}_0^{-1} : \mathbb{c}_r - \mathbb{I} \right) \right]^{-1} \right\} \\ &\quad : \left\{ \sum_{r \in 0,i} f_r \left[\mathbb{I} + \mathbb{S}_r : \left(\mathbb{c}_0^{-1} : \mathbb{c}_r - \mathbb{I} \right) \right]^{-1} \right\}^{-1} \end{aligned} \tag{20}$$

Eq. (20) can be extended to multiple types of inclusions, reading

$$\begin{aligned} \mathbb{C}_{eff} = &\left\{ \sum_r f_r \mathbb{c}_r : \left[\mathbb{I} + \mathbb{S}_r : \left(\mathbb{c}_0^{-1} : \mathbb{c}_r - \mathbb{I} \right) \right]^{-1} \right\} : \\ &\left\{ \sum_r f_r \left[\mathbb{I} + \mathbb{S}_r : \left(\mathbb{c}_0^{-1} : \mathbb{c}_r - \mathbb{I} \right) \right]^{-1} \right\}^{-1} \end{aligned} \tag{21}$$

with $r \in$ {matrix material = reference medium 0, inclusion 1, inclusion 2, ... } for the case of the MT scheme and $r \in$ {material phases } in case of the SC scheme with the material tensor of the reference medium $\mathbb{c}_0$ set equal to the effective material tensor $\mathbb{C}_{eff}$. In the following, Eq. (21) is specialized for the application to cement-based materials, characterized by isotropic material behavior. Thus, Eq. (21) can be reduced to the specification of the effective shear and bulk modulus, μ_{eff} and k_{eff}, respectively:

- For the SC scheme,

$$\mu_{eff} = \frac{\sum_r f_r \mu_r \left[1 + \beta \left(\frac{\mu_r}{\mu_{eff}} - 1 \right) \right]^{-1}}{\sum_r f_r \left[1 + \beta \left(\frac{\mu_r}{\mu_{eff}} - 1 \right) \right]^{-1}}$$

and (22)

$$k_{eff} = \frac{\sum_r f_r k_r \left[1 + \alpha \left(\frac{k_r}{k_{eff}} - 1 \right) \right]^{-1}}{\sum_r f_r \left[1 + \alpha \left(\frac{k_r}{k_{eff}} - 1 \right) \right]^{-1}}$$

where α and β represent the volumetric and deviatoric part of the Eshelby tensor $\mathbb{S}$ specialized for spherical inclusions, reading

$$\alpha = \frac{3k_{eff}}{3k_{eff} + 4\mu_{eff}} \quad \text{and} \quad \beta = \frac{6\left(k_{eff} + 2\mu_{eff}\right)}{5\left(3k_{eff} + 4\mu_{eff}\right)} \tag{23}$$

[*3] *Levin's* theorem states that the effective state equation is of the same form as the local state equation (Zaoui 1997).

[*4]

$$\begin{aligned} f_0 \left\langle \mathbb{A}(\mathrm{x}) \right\rangle_{\mathrm{V}_0} &= \mathbb{I} - f_i [\square]^{-1} : \{\bullet\}^{-1} \\ &= \{\bullet\} : \{\bullet\}^{-1} - f_i [\square]^{-1} : \{\bullet\}^{-1} \\ &= \left(\{\bullet\} - f_i [\square]^{-1} \right) : \{\bullet\}^{-1} \\ &= (f_0 [\mathbb{I} + \mathbb{S}_0 : (\mathbb{c}_0^{-1} : \mathbb{c}_0 - \mathbb{I})]^{-1} \\ &\quad + f_i [\square]^{-1} - f_i [\square]^{-1}) : \{\bullet\}^{-1} \\ &= f_0 \{\bullet\}^{-1} \end{aligned} \tag{18}$$

with the abbreviations

$$\{\bullet\} = \left\{ \sum_{r=0,i} f_r [\mathbb{I}\mathbb{S}_r : (\mathbb{c}_0{}^{-1} : \mathbb{c}_r - \mathbb{I})]^{-1} \right\} \text{ and}$$

$$[\square] = \left[\mathbb{I} + \mathbb{S}_i : (\mathbb{c}_0{}^{-1} : \mathbb{c}_i - \mathbb{I}) \right]$$

- For the MT scheme,

$$\mu_{eff} = \frac{\sum_r f_r \mu_r \left[1+\beta\left(\frac{\mu_r}{\mu_m}-1\right)\right]^{-1}}{\sum_r f_r \left[1+\beta\left(\frac{\mu_r}{\mu_m}-1\right)\right]^{-1}}$$

and (24)

$$k_{eff} = \frac{\sum_r f_r k_r \left[1+\alpha\left(\frac{k_r}{k_m}-1\right)\right]^{-1}}{\sum_r f_r \left[1+\alpha\left(\frac{k_r}{k_m}-1\right)\right]^{-1}}$$

with

$$\alpha = \frac{3k_m}{3k_m+4\mu_m} \quad \text{and} \quad \beta = \frac{6(k_m+2\mu_m)}{5(3k_m+4\mu_m)} \tag{25}$$

Applying the SC scheme to Scale Ia, the different material phases are given by $r \in$ {clinker phases C_3S, C_2S, C_3A, C_4AF}. The MT scheme is applied at Scales Ib.1, Ib.2, II, and III with the material phases given by $r \in$ {matrix material m and multiple inclusions, such as, e.g., water and air at Scale Ib.2 }. In Eqs. (24) and (25), the material matrix m is represented by low-density CSH at Scale Ib.1, the homogenized material determined at Scale Ib.1 at Scale Ib.2, the homogenized material determined at Scale Ib.2 at Scale II, and the homogenized material determined at Scale II at Scale III. **Figure 3** shows a comparison of the elastic properties predicted by the multiscale model and test results for shotcrete, using the finer-scale input listed in **Appendix 2(a)**). Hereby, the effective Poisson's ratio, v_{eff}, is continuously decreasing in case the bulk modulus of water is set to k_w =2.3GPa, starting from an initial value of 0.5. For k_w =0, on the other hand, v_{eff} is continuously increasing (see **Fig. 4**).

4. Upscaling of creep properties

Viscous material response is characterized by (i) an increase of deformation during constant loading (creep) and (ii) a decrease of stress for constraint deformation (relaxation). The viscous response is commonly described by the creep compliance J [Pa^{-1}] and the relaxation modulus R [Pa] , both dependent on time. The creep compliance associated with uniaxial loading is determined as

$$J(t) = \frac{\varepsilon(t)}{\sigma_0} \tag{26}$$

with $\varepsilon(t)$ denoting the measured strain, and σ_0 representing the applied constant stress. The relaxation modulus, on the other hand, is determined from the

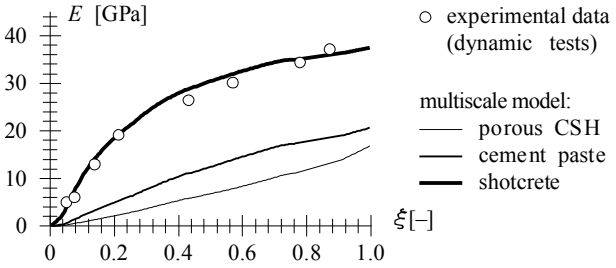

Fig. 3 Comparison between test results (Lackner *et al*. 2002b) and multiscale model for upscaling of elastic properties for shotcrete employed at the Lainzer tunnel (see Appendix 2(a)) for isothermal conditions. (T = const. =11℃).

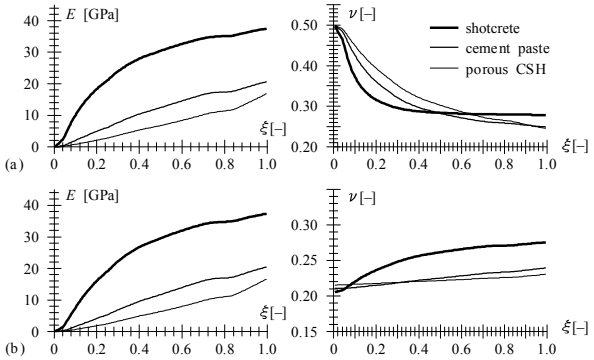

Fig. 4 Result from upscaling of elastic properties for shotcrete employed at the Lainzer tunnel (see Appendix 2(a)) for isothermal conditions (T = const. = 20℃) considering (a) k_w = 2.3 GPa and (b) k_w = 0.

measured stress decrease $\sigma(t)$ in consequence of a constant strain ε_0 as

$$R(t) = \frac{\sigma(t)}{\varepsilon_0} \tag{27}$$

Introducing the Boltzmann convolution integral, Eqs. (26) and (27) can be expanded towards variable (non-constant) stress or strain histories, respectively:

$$\varepsilon(t) = \int_0^t J(t-\tau)\frac{\partial\sigma(\tau)}{\partial\tau}d\tau \quad \text{and}$$

$$\sigma(t) = \int_0^t R(t-\tau)\frac{\partial\varepsilon(\tau)}{\partial\tau}d\tau \tag{28}$$

where τ denotes the time instant of loading. Applying the Laplace transform[*5] to Eqs. (28) gives

$$\hat{\varepsilon}(p) = p\hat{J}(p)\hat{\sigma}(p) \quad \text{and} \quad \hat{\sigma}(p) = p\hat{R}(p)\hat{\varepsilon}(p),$$

$$\text{with} \quad p\hat{J}(p) = \frac{1}{p\hat{R}(p)} \tag{32}$$

considering that the Laplace transform of the convolution integral becomes a multiplication and $\partial\varepsilon/\partial\tau$ turns into $p\hat{\varepsilon}$. Considering the definition of the Laplace-Carson transformation as $f^\star = p\hat{f}$ in Eqs. (32) yields

$$\varepsilon^\star(p) = J^\star(p)\sigma^\star(p) \quad \text{and} \quad \sigma^\star(p) = R^\star(p)\varepsilon^\star(p),$$
$$\text{with} \quad J^\star(p) = \frac{1}{R^\star(p)} \tag{33}$$

The analogous form of $\sigma^\star = R^\star\varepsilon$ in Eq. (33) and the elastic constitutive law $\sigma = E\varepsilon$ is the basis for the "correspondence principle" (Lee 1955; Mandel 1966; Laws and McLaughlin 1978). According to this principle, viscoelastic problems are solved using the respective solution of the elastic problem in the Laplace-Carson domain.

The *Laplace-Carson transform method* (Lee 1955) for the solution of linear viscoelastic boundary value problems (BVPs) is characterized by the elimination of the time dependence by applying the Laplace-Carson transform to the field equation (which contains the time dependent moduli) as well as the boundary conditions, and solving the "corresponding" elastic problem in the Laplace-Carson domain[*6]. The application of the Laplace-Carson transform method is restricted to BVPs with the location of the boundary conditions in tractions and displacements fixed in time. Hence, the method can be adopted for derivation of viscoelastic homogenization schemes, which are based on an inclusion embedded in an (infinite) matrix with homogeneous boundary conditions as it is the case in the framework of continuum micromechanics. Applying this method, the elastic material parameters, e.g., the shear compliance $J^{dev} = 1/\mu$, where μ is the shear modulus, are replaced by the Laplace-Carson transform of the respective viscoelastic material parameters, e.g., the Laplace-Carson transform of the creep compliance associated with deviatoric creep $J^{dev\star}$. The solution of the viscoelastic problem in the time domain is obtained by inverse Laplace-Carson transformation. E.g., application of the correspondence principle to the MT scheme introduced for upscaling of elastic properties in Section 3 gives access to the effective creep compliance of matrix-inclusion type composites (see, e.g., Beurthey and Zaoui (2000) for an application of the correspondence principle to the self-consistent scheme).

As outlined in the Section 1, viscoelastic behavior of cement-based materials originates from dislocation-like processes within CSH. Hence, as for homogenization at Scale Ib-2, viscoelastic material behavior is assigned to the matrix material (CSH), while the inclusions (water, air) exhibit elastic deformations only. Motivated by the macroscopic observation that, after a period of rapid decrease, the compliance rate of cement-based materials follows $\dot{J} \sim 1/t$ (Ulm *et al.* 1999) (see, e.g., experimental results in Acker and Ulm (2001)), a logarithmic-type deviatoric creep law is employed to describe creep of CSH:

$$J^{dev}_{CSH}(t-\tau) = \frac{1}{\mu_{CSH}} + J^{v,dev}_{CSH} \ln\left[1 + \frac{t-\tau}{\tau^{v,dev}_{CSH}}\right] \tag{34}$$

Volumetric creep of CSH, on the other hand, is omitted. In addition to observations at the macroscale, this *type* of creep law was also found at the μm-scale of observation by means of nanoindentation tests (Pichler and Lackner 2007).

The Laplace-Carson transform of the deviatoric creep compliance of CSH given in Eq. (34) reads

$$\begin{aligned} J^{dev\star}_{CSH} &= \mathfrak{LC}\left[J^{dev}_{CSH}(t-\tau)\right] \\ &= \frac{1}{\mu_{CSH}} + J^{v,dev}_{CSH} \exp\left[p\tau^{v,dev}_{CSH}\right]\Gamma\left[0, p\tau^{v,dev}_{CSH}\right] \end{aligned} \tag{35}$$

with Γ denoting the incomplete gamma-function[*7]. Applying the correspondence principle to the effective creep compliance obtained by the MT scheme [Eq. (24.1)], the Laplace-Carson transform of the effective deviatoric creep compliance at Scale Ib.2 is obtained as

$$J^{dev\star}_{eff} = \frac{\sum_r f_r \left[1 + \beta^\star\left(\frac{J^{dev\star}_m}{J^{dev\star}_r} - 1\right)\right]^{-1}}{\sum_r \frac{f_r}{J^{dev\star}_r}\left[1 + \beta^\star\left(\frac{J^{dev\star}_m}{J^{dev\star}_r} - 1\right)\right]^{-1}} \tag{37}$$

with $r \in \{m = \text{CSH, air, water}\}$.
In Eqs. (37),

[*5] Whereas the Laplace transformation of $f(t)$ is defined as

$$\mathfrak{L}[f(t)] = \hat{f}(p) = \int_0^\infty f(t)e^{-pt}dt \tag{29}$$

with p as the complex variable, the Laplace-Carson transformation of $f(t)$ is given as

$$\mathfrak{LC}[f(t)] = f^\star(p) = p\int_0^\infty f(t)e^{-pt}dt \tag{30}$$

Hence, $f^\star(p) = p\hat{f}(p)$. The inverse Laplace-Carson transformation is defined in the complex plane as

$$\mathfrak{LC}^{-1}[f^\star(p)] = f(t) = \frac{1}{2i\pi}\int_\Omega \frac{f^\star(p)}{p}e^{pt}dp \tag{31}$$

where Ω is a parallel to the imaginary axis having all poles of $f^\star(p)$ to the left.

[*6] Hence, this method is restricted to BVPs with boundary conditions admitting such an operation.

[*7] The incomplete gamma function $\Gamma[a, z]$ satisfies

$$\Gamma[a, z] = \int_z^\infty t^{a-1}e^{-t}dt \tag{36}$$

$$\beta^{\star}=\frac{6\left(1/J_m^{vol\star}+2/J_m^{dev\star}\right)}{5\left(3/J_m^{vol\star}+4/J_m^{dev\star}\right)} \tag{38}$$

represents the deviatoric part of the (Laplace-Carson transformed) Eshelby tensor specialized for spherical inclusions. In Eqs. (37) and (38), $J_r^{dev\star}=1/\mu$ and $J_m^{dev\star}=1/k_m$ for the case of elastic material response. Inserting Eq. (35) into Eq. (37) and performing the inverse Laplace-Carson transformation gives access to the effective deviatoric creep compliance, $J_{eff}^{dev}(t)=\mathcal{LC}^{-1}[J_{eff}^{dev\star}]$. Hereby, the inverse transformation was performed in a pointwise manner (for discrete values of $t>0$) by applying the Gaver-Stehfest algorithm (Stehfest 1970). Implying an affine form of the creep compliance of CSH, J_{CSH}^{dev} [see Eq. (34)], and the effective creep compliance, $J_{eff}^{dev}(t)$, respectively, the discrete points from inverse transformation are approximated by

$$J_{eff}^{dev}\left(t-\tau\right)=\frac{1}{\mu_{eff}\left[\xi\left(\tau\right)\right]}+J_{eff}^{v,dev}\left[\xi\left(\tau\right)\right]\ln\left(1+\frac{t-\tau}{\tau_{eff}^{v,dev}\left[\xi\left(\tau\right)\right]}\right) \tag{39}$$

giving access to the effective creep parameters $J_{eff}^{v,dev}[\xi(\tau)]$ and $\tau_{eff}^{v,dev}[\xi(\tau)]$ [see **Fig. 5(a)**]. In Eq. (39), $\mu_{eff}[\xi(\tau)]$ is the effective shear modulus determined according to Eq. (24.1). Examining the volumetric part of the Eshelby tensor specialized for spherical inclusions, with

$$\alpha^{\star}=\frac{3/J_m^{vol\star}}{3/J_m^{vol\star}+4/J_m^{dev\star}} \tag{40}$$

deviatoric creep in the matrix material (CSH) triggers (effective) volumetric creep deformations at Scale Ib.2. The Laplace-Carson transform of the effective volumetric creep compliance is obtained as

$$J_{eff}^{vol\star}=\frac{\sum_r f_r\left[1+\alpha^{\star}\left(\frac{J_m^{vol\star}}{J_r^{vol\star}}-1\right)\right]^{-1}}{\sum_r \frac{f_r}{J_r^{vol\star}}\left[1+\alpha^{\star}\left(\frac{J_m^{vol\star}}{J_r^{vol\star}}-1\right)\right]^{-1}} \tag{41}$$

with $r\in\{m=\text{CSH, air, water}\}$,

where $J_r^{vol\star}=1/k_r$ for the case of elastic material response. After applying the inverse Laplace-Carson transformation (Stehfest 1970) to Eq. (41), the discrete points were approximated by

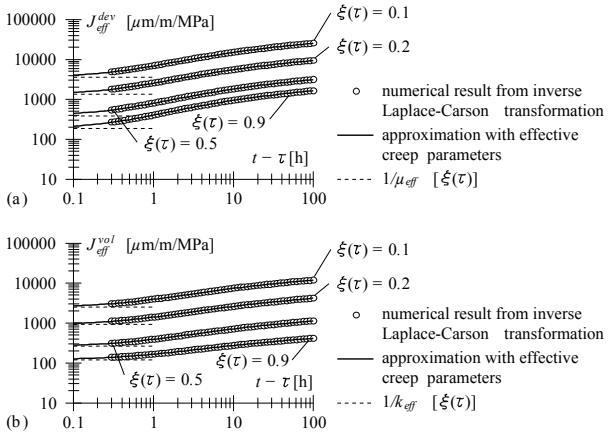

Fig. 5 Approximation of effective creep compliance obtained from inverse Laplace-Carson transformation at Scale Ib.2 for different hydration extents (using $J_{CSH}^{v,dev}$ =0.175 GPa^{-1} and $\tau_{CSH}^{v,dev}$ =1 h).

$$J_{eff}^{vol}\left(t-\tau\right)=\frac{1}{k_{eff}\left[\xi\left(\tau\right)\right]}+J_{eff}^{v,vol}\left[\xi\left(\tau\right)\right]\ln\left(1+\frac{t-\tau}{\tau_{eff}^{v,vol}\left[\xi\left(\tau\right)\right]}\right) \tag{42}$$

[see **Fig. 5(b)**]. Hereby, $k_{eff}[\xi(\tau)]$ is the effective bulk modulus determined according to Eq. (24.2). The effective creep parameters $J_{eff}^{v,dev}[\xi(\tau)]$, $J_{eff}^{v,vol}[\xi(\tau)]$, $\tau_{eff}^{v,dev}[\xi(\tau)]$, and $\tau_{eff}^{v,vol}[\xi(\tau)]$ [see Eqs. (39) and (42)] define the matrix behavior at the next higher scale of observation (Scale II). At this scale, the homogenization procedure described above [Eqs. (37) to (42)] is applied accordingly, with the material phases $r\in$ {matrix m as the effective material determined at Scale Ib.2; inclusions: anhydrous cement, gypsum, monosulfate, ettringite, portlandite, $C_3(A,F)H_6$}. The effective creep parameters determined at Scale II serve as input for material matrix at Scale III, where the material phases $r\in$ {matrix m and aggregates} and the homogenization procedure is applied once more. Hereby, inverse Laplace-Carson transformation is performed, equally to Scale Ib.2, in a point-wise manner, with subsequent approximation according to Eqs. (39) and (42) (see **Fig. 6**). **Figure 7** illustrates the described upscaling procedure for the shotcrete already considered in **Fig. 4** (see in **Appendix 2(a)**), giving access to the effective creep parameters $J_{eff}^{v,dev}(\xi)$, $J_{eff}^{v,vol}(\xi)$, $\tau_{eff}^{v,dev}(\xi)$, and $\tau_{eff}^{v,vol}(\xi)$.

Early-age cement-based materials are characterized by a continuously changing microstructure, i.e., the volume fractions of the material phases at the respective scale of observation change with the hydration extent. At Scale Ib.2, e.g., the volume fraction of creep-active CSH increases, while the water fraction is continuously decreasing. The dependence of the creep parameters on the

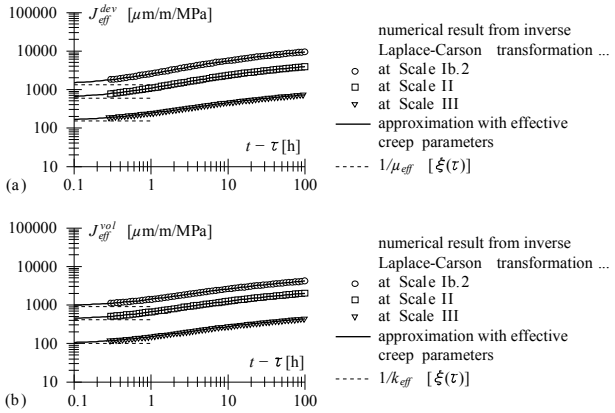

Fig. 6 Approximation of effective creep compliance obtained from inverse Laplace-Carson transformation for $\xi(\tau) = 0.2$ (using $J_{CSH}^{v,dev}$ =0.175 GPa^{-1} and $\tau_{CSH}^{v,dev}$ =1 h).

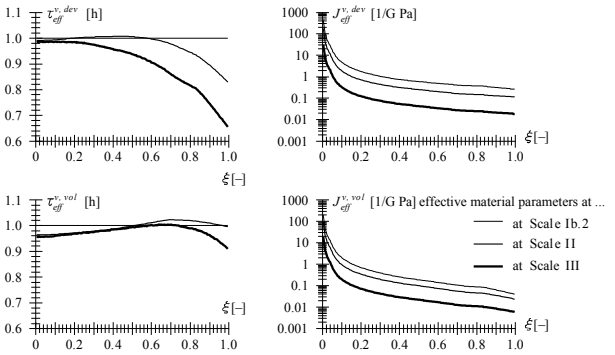

Fig. 7 Effective creep parameters for shotcrete employed at the Lainzer tunnel [see Appendix 2(a)] (using $J_{CSH}^{v,dev}$ =0.175 GPa^{-1} and $\tau_{CSH}^{v,dev}$ =1 h).

hydration extent and, thus, on the time is considered by the reformulation of the Boltzmann convolution integral [Eq. (28)] in terms of the creep-compliance rate $\dot{\mathbb{J}}$, giving the viscous part of the strain tensor in the form

$$\boldsymbol{\varepsilon}^{v}(t) = \int_0^t \left\{ \int_\tau^t \dot{\mathbb{J}}^{v,age}\left[\hat{t}-\tau, \xi(\hat{t})\right] d\hat{t} \right\} : \frac{\partial \boldsymbol{\sigma}(\tau)}{\partial \tau} d\tau \quad (43)$$

where $\dot{\mathbb{J}}^{v,age}$ denotes the aging creep-compliance rate, with

$$\dot{\mathbb{J}}^{v,age}\left[\hat{t}-\tau, \xi(\hat{t})\right] = \frac{1}{3}\mathbb{I}^{vol} \frac{J_{eff}^{v,vol}\left[\xi(\hat{t})\right]}{\hat{t}-\tau+\tau_{eff}^{v,vol}\left[\xi(\hat{t})\right]} + \frac{1}{2}\mathbb{I}^{dev} \frac{J_{eff}^{v,dev}\left[\xi(\hat{t})\right]}{\hat{t}-\tau+\tau_{eff}^{v,dev}\left[\xi(\hat{t})\right]} \quad (44)$$

In Eq. (44), $\mathbb{I}^{vol}$ and $\mathbb{I}^{dev}$ are defined as

$$\mathbb{I}^{vol} = \begin{bmatrix} 1/3 & 1/3 & 1/3 & 0 & 0 & 0 \\ 1/3 & 1/3 & 1/3 & 0 & 0 & 0 \\ 1/3 & 1/3 & 1/3 & 0 & 0 & 0 \\ 0 & 0 & 0 & 0 & 0 & 0 \\ 0 & 0 & 0 & 0 & 0 & 0 \\ 0 & 0 & 0 & 0 & 0 & 0 \end{bmatrix} \quad (45)$$

and

$$\mathbb{I}^{dev} = \begin{bmatrix} 2/3 & -1/3 & -1/3 & 0 & 0 & 0 \\ -1/3 & 2/3 & -1/3 & 0 & 0 & 0 \\ -1/3 & -1/3 & 2/3 & 0 & 0 & 0 \\ 0 & 0 & 0 & 1 & 0 & 0 \\ 0 & 0 & 0 & 0 & 1 & 0 \\ 0 & 0 & 0 & 0 & 0 & 1 \end{bmatrix} \quad (46)$$

Figure 8 compares the *non-aging* creep-compliance rate[*8] with the *aging* creep-compliance rate according to Eq. (44) for uniaxial loading and different time instants of loading τ, corresponding to $\xi(\tau)$=0.2, 0.4, 0.6, and 0.8.

During hydration of concrete, new hydration products are formed in a state free of microstress (Bažant 1979), and loaded exclusively by stresses applied after formation. This situation is accounted for by an incremental stress-strain law for the elastic part of the strain reading

$$\begin{aligned} d\boldsymbol{\varepsilon}^{e}(\tau) &= \mathbb{C}^{-1}\left[\xi(\tau)\right] : d\boldsymbol{\sigma}(\tau) \\ &= \left\{ \frac{1}{3}\mathbb{I}^{vol} \frac{1}{k_{eff}\left[\xi(\tau)\right]} + \frac{1}{2}\mathbb{I}^{dev} \frac{1}{\mu_{eff}\left[\xi(\tau)\right]} \right\} : d\boldsymbol{\sigma}(\tau) \end{aligned} \quad (48)$$

giving the total strain tensor as

$$\begin{aligned} \boldsymbol{\varepsilon}(t) &= \boldsymbol{\varepsilon}^{e}(t) + \boldsymbol{\varepsilon}^{v}(t) \\ &= \int_0^t \left\{ \left[\mathbb{C}^{-1}\left[\xi(\tau)\right] + \int_\tau^t \dot{\mathbb{J}}^{v,age}\left[\hat{t}-\tau, \xi(\hat{t})\right] d\hat{t} \right\} : \frac{\partial \boldsymbol{\sigma}(\tau)}{\partial \tau} d\tau \end{aligned} \quad (49)$$

[*8] The *non-aging* creep-compliance rate is determined (for sake of comparison) as

$$\begin{aligned} \dot{\mathbb{J}}^{v,non\ aging}(t-\tau) &= \frac{1}{3}\mathbb{I}^{vol} j_{eff}^{v,vol}(t-\tau) + \frac{1}{2}\mathbb{I}^{dev} j_{eff}^{v,dev}(t-\tau) \\ &= \frac{1}{3}\mathbb{I}^{vol} \frac{j_{eff}^{v,vol}[\xi(\tau)]}{t-\tau+\tau_{eff}^{v,vol}[\xi(\tau)]} + \frac{1}{2}\mathbb{I}^{dev} \frac{j_{eff}^{v,dev}[\xi(\tau)]}{t-\tau+\tau_{eff}^{v,dev}[\xi(\tau)]} \end{aligned} \quad (47)$$

where τ is the time instant of loading.

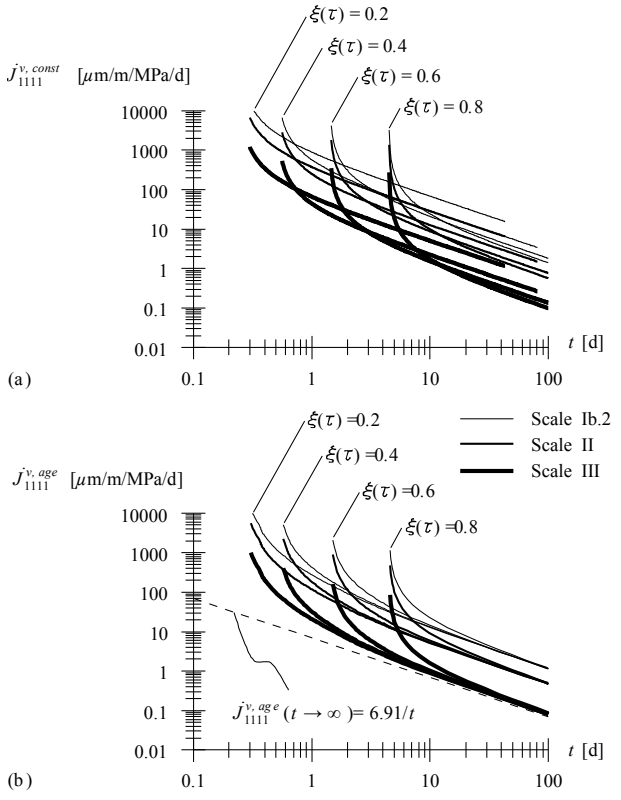

Fig. 8 Comparison between (a) uniaxial *non-aging* creep-compliance rate [see Equation (47)] and (b) uniaxial *aging* creep-compliance rate [see Equation (44)] ($J^{v,dev}_{CSH}$ =0.175 GPa^{-1} and $\tau^{v,dev}_{CSH}$ =1 h).

5. Identification of creep parameters

5.1 Identification of $J^{v,dev}_{CSH}$ and $\tau^{v,dev}_{CSH}$

In order to determine the intrinsic creep parameters of CSH, $J^{v,dev}_{CSH}$ and $\tau^{v,dev}_{CSH}$, macroscopic creep tests are used in conjunction with the described multiscale model. For this purpose, a top-down application of the presented multiscale model is applied by adapting the finer-scale intrinsic input parameters aiming at a correct prediction of the macroscopic creep data. **Figure 9** shows the time-dependent part of the employed deviatoric creep compliance for CSH, $J^{v,dev}_{CSH} \ln[1 + (t - \tau)/\tau^{v,dev}_{CSH}]$ [see Eq. (34)] for different time instants of loading τ, given by $\tau / \tau^{v,dev}_{CSH}$. Taking the derivative of Eq. (34), giving

$$\dot{J}^{dev}_{CSH} = \frac{J^{v,dev}_{CSH}}{t - \tau + \tau^{v,dev}_{CSH}} \tag{50}$$

and specializing Eq. (50) for $(t - \tau) \gg \tau^{v,dev}_{CSH}$ gives access to the long-term asymptote of the creep-compliance rate as

$$\dot{J}^{dev}_{CSH}\Big|_{(t-\tau)\gg\tau^{v,dev}_{CSH}} = \frac{J^{v,dev}_{CSH}}{t - \tau} \tag{51}$$

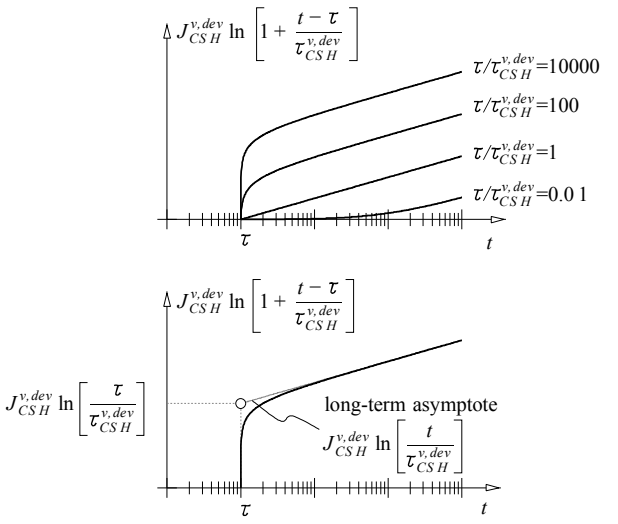

Fig. 9 Illustration of time-dependent part of $J^{dev}_{CSH}(t - \tau)$ (see Equation (34)) for different time instants of loading τ (given by $\tau / \tau^{v,dev}_{CSH}$).

Hence, the long-term creep-compliance rate is solely controlled by $J^{v,dev}_{CSH}$, while the short-term creep-compliance rate is controlled by both parameters, with

$$\dot{J}^{dev}_{CSH}\Big|_{(t-\tau)=0} = \frac{J^{v,dev}_{CSH}}{\tau^{v,dev}_{CSH}} \tag{52}$$

Accordingly, $J^{v,dev}_{CSH}$ may be adapted in order to fit the long-term response of macroscopic test data, while $\tau^{v,dev}_{CSH}$ is adjusted to match the creep-compliance rate directly after application of the load. Experimental results given in Hummel *et al*. (1962) and Athrushi (2003) are employed to identify $J^{v,dev}_{CSH}$ and $\tau^{v,dev}_{CSH}$. Whereas the best agreement between multiscale model and experimental data reported in Hummel *et al*. (1962) is obtained for $J^{v,dev}_{CSH}$ = 0.175 GPa^{-1} and $\tau^{v,dev}_{CSH}$ = 3 h, $J^{v,dev}_{CSH}$ = 0.105 GPa^{-1} and $\tau^{v,dev}_{CSH}$ = 3/4 h give the best agreement when using experimental data from Athrushi (2003) [see Pichler (2007)].

5.2 Discussion

The variation of $J^{v,dev}_{CSH}$ highlighted in the previous section may be explained by the different environmental conditions present at the creep tests. Whereas both test series were conducted under isothermal conditions (T=20℃), the specimens tested in Hummel *et al*. (1962) were subjected to a relative humidity h of 100% for the age <7d and h = 65% for an age >7 d. The tests reported in Athrushi (2003), on the other hand, are characterized by h =50%. Hence, the larger the humidity h, the larger $J^{v,dev}_{CSH}$ and, consequently, the larger the macroscopically-observed long-term compliance rate. The variation in the identified values for $\tau^{v,dev}_{CSH}$ suggests a dependence of $\tau^{v,dev}_{CSH}$ on the degree of hydration. According to Ruetz

(1966); Wittmann (1982); Ulm (1998), the short-term creep behavior is associated with stress-induced micro-diffusion of water in the capillary pores. Hereby, the underlying diffusion process may depend on the capillary depression p_c and the permeability of the solid skeleton, both of them depending on the hydration extent. Based on the determination of capillary depression in the water phase $p_c(\xi)$ (Pichler *et al*. 2007), a dependence of $\tau_{CSH}^{v,dev}$ on the hydration extent is proposed as

$$\tau_{CSH}^{v,dev}(\xi) = \tau_{CSH,\infty}^{v,dev} \frac{p_c(\xi)}{p_c(h_{\exp})} \tag{53}$$

with $p_c(h_{exp})$ as the capillary depression related to the relative humidity h_{exp} of the medium surrounding the sample during the experiment via *Kelvin's* equation[*9]. The best agreement between the creep compliance predicted by the multiscale model and experimental data (Hummel *et al*. 1962; Athrushi 2003) was found when setting $\tau_{CSH,\infty}^{v,dev}$ =4 d in Eq. (53), with h_{exp} = 0.65 for the experiments given in Hummel *et al*. (1962) and h_{exp} =0.5 characterizing the experimental results given in Athrushi (2003).

The uniaxial creep tests given in Laplante (1993) have frequently been used to calibrate macroscopic creep formulations (see, e.g., Sercombe *et al*. (2000); Cervera *et al*. (1999)). These tests are characterized by h_{exp} = 50%, with the input parameters for the multiscale model being summarized in **Appendix 2(b)**. When using parts of the data sets reported in Hummel *et al*. (1962); Athrushi (2003); Laplante (1993) characterized by a certain *w*/*c*-ratio for top-down identification of $J_{CSH}^{v,dev}$, a dependency of $J_{CSH}^{v,dev}$ on h_{exp} *and* the *w*/*c*-ratio is observed (see **Figs. 10** and **11**), with higher values of $J_{CSH}^{v,dev}$ for increasing h_{exp} and decreasing *w*/*c*-ratio. Consequently, CSH formed at a lower *w*/*c*-ratio has a greater creep compliance, which may be explained by more pronounced "intrinsic" microcracking / damage in CSH formed at lower *w*/*c*-ratios, yielding higher compliance under sustained loading[*10] (see **Fig. 12**). Nanoindentation tests on well hydrated cement paste samples (Pichler and Lackner 2007) reveal a logarithmic-type creep behavior with a mean value for $J^{v,dev}$ of approximately 0.04 GPa^{-1} for *w*/*c* = 0.4 and h_{exp} = 50%. This value is lower than the respective value obtained from top-down identification of $J_{CSH}^{v,dev}$ as a function of *w*/*c* and h_{exp},

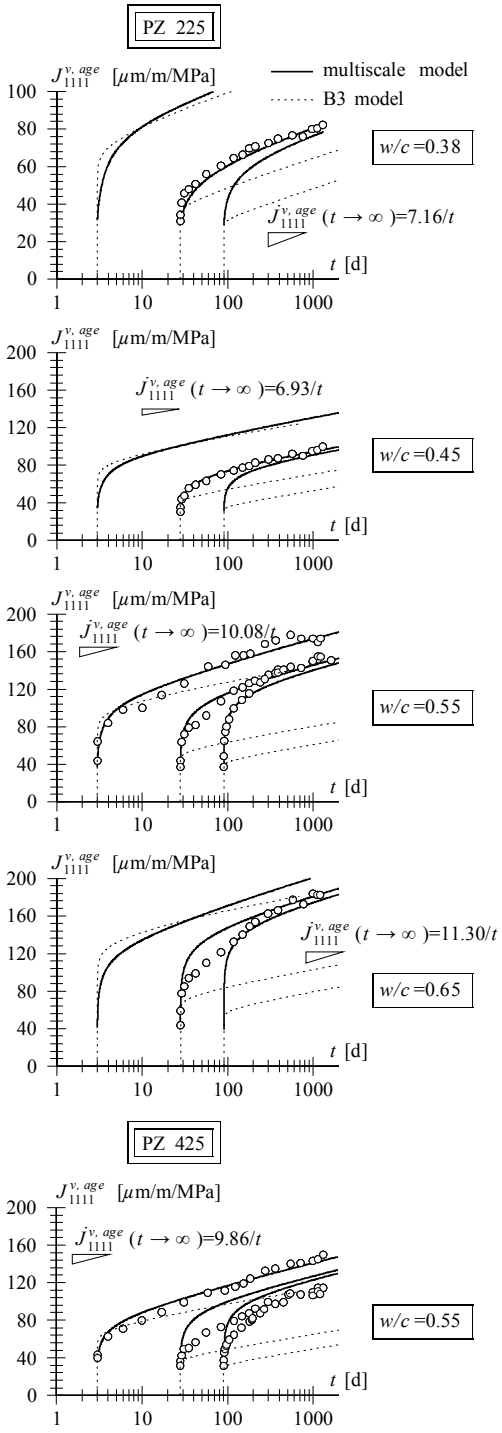

Fig. 10 Top-down identification of $J_{CSH}^{v,dev}$ and $\tau_{CSH}^{v,dev}$ from experimental data given in Hummel et al. (1962) (see Appendix 2(c)) and comparison with B3 model (Bažant and Baweja 1997) ($J_{CSH}^{v,dev}$ (*w*/*c*=0.38) = 0.315 GPa^{-1}, $J_{CSH}^{v,dev}$ (*w*/*c*=0.45) = 0.200 GPa^{-1}, $J_{CSH}^{v,dev}$ (*w*/*c*=0.55)= 0.175GPa^{-1}, $J_{CSH}^{v,dev}$ (*w*/*c*=0.65) = 0.130 GPa^{-1}, $\tau_{CSH,\infty}^{v,dev}$ =4 d)

[*9] *Kelvin's equation* expresses the liquid-vapor equilibrium under atmospheric conditions:

$$p_c = -\frac{\rho_H RT}{M_H} \ln h \tag{54}$$

where ρ_H =998 kg/m^3 is the density of water, R=8.3144 J/(mol K) is the universal gas constant, T is the absolute temperature, M_H=0.018 kg/mol is the molar mass of water, and h is the relative humidity.

[*10] Though not directly related, the study in Neubauer and Jennings (2000) contains a microstructural investigation of shrinking cement paste during drying. Hereby, large local deformation is associated with the collapse of the colloidal network of CSH. The observed damage (fracture) is more pronounced in stiffer samples, i.e., in samples with lower *w*/*c* ratio.

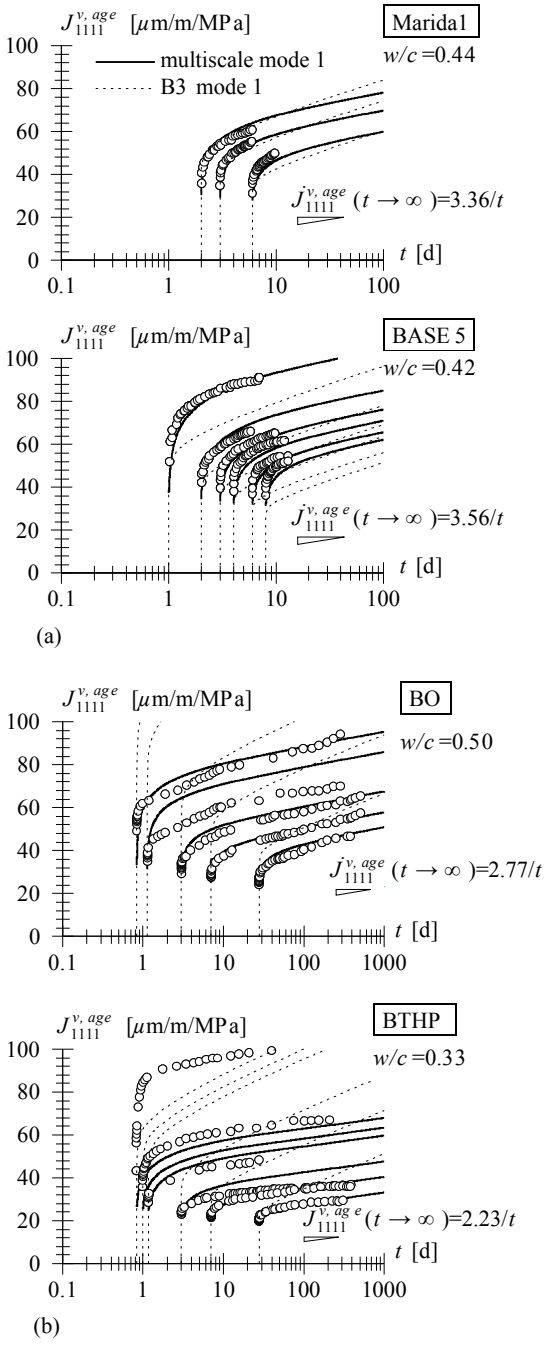

Fig. 11 Top-down identification of $J_{CSH}^{v,dev}$ and $\tau_{CSH}^{v,dev}$ from experimental data given in (a) Athrushi (2003) ("BASE5" [$J_{CSH}^{v,dev}$ =0.120 GPa^{-1}] and "Maridal" [$J_{CSH}^{v,dev}$ =0.105 GPa^{-1}], see Appendix 2(c)), and (b) Laplante (1993) ("BO" [$J_{CSH}^{v,dev}$ =0.060 GPa^{-1}] and "BTHP" [$J_{CSH}^{v,dev}$ =0.100 GPa^{-1}], see Appendix 2(b)), [$\tau_{CSH,\infty}^{v,dev}$ =4 d], comparison with B3 model (Bažant and Baweja 1997)

giving approximately 0.09 GPa^{-1} (see **Fig. 12**), which is explained by the nanoindentation penetration depth of approximately 250 nm and the corresponding contact area of (1.4 μm)^2 π /4 = 1.5 μm^2, lying within Scales I and II (see **Fig. 1**).

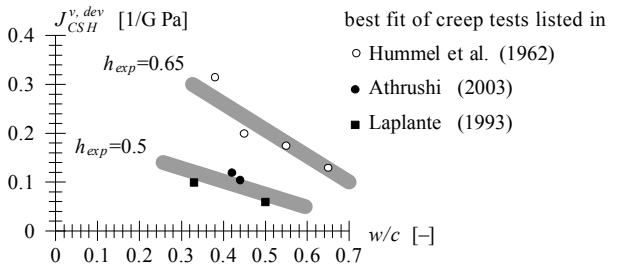

Fig. 12 Top-down identification of $J_{CSH}^{v,dev}$ being a function of *w/c* and h_{exp}.

Appendix A summarizes the algorithmic treatment of the logarithmic-type creep model for early-age cement-based materials in nonlinear FE analyses employed in Section 6 for the hybrid analysis of shotcrete tunnel linings.

6. Application to tunnel lining analysis

Themultiscale model presented in the previous sections is employed in the context of hybrid analyses of shotcrete tunnel linings used as primary support during tunneling according to the New Austrian Tunneling Method (NATM) (Lackner *et al*. 2006; Lackner and Mang 2003). This analysis scheme combines in-situ displacement measurements in measurement points (MPs), which are fixed to the tunnel lining and arranged in so-called measurement cross-sections (MCSs), with a thermo-chemomechanical material model for shotcrete. Within this macroscopic material model, stiffness growth, autogenous shrinkage, and creep are specified by means of intrinsic material functions, giving material parameters as a function of the degree of hydration ξ, which are provided by the proposed multiscale model.

In the present application, one MCS of the Lainzer tunnel near Vienna, which was constructed as part of the high-capacity railway from Vienna to Salzburg, is investigated (MCS at km 8.340 of track 9). The geometric dimensions of this part of the Lainzer tunnel are given in **Fig. 13**. The necessary input parameters for the multiscale model are summarized in **Appendix 2(a)**, giving access to the intrinsic material functions for Young's modulus $E(\xi)$, Poisson's ratio $\nu(\xi)$, creep parameters $J^{v,dev}(\xi)$, $J^{v,vol}(\xi)$, $\tau^{v,dev}(\xi)$, and $\tau^{v,vol}(\xi)$, and autogenous-shrinkage strain $\varepsilon^s(\xi)$ [see thick solid lines in **Figs. 14(a)** to **(g)**]. For determination of creep parameters, $\tau_{CSH,\infty}^{v,dev}$ was set to 4 d, whereas $J_{CSH}^{v,dev}$ was set to 0.075 GPa^{-1}. The intrinsic material function for the strength growth, on the other hand, is obtained from macroscopic experiments (Lackner and Mang 2003) [see **Fig. 14(h)**]. Shotcrete employed at this part of the Lainzer tunnel is characterized by a *w*/*c*-ratio of 0.48. In order to assess the influence of the *w*/*c*-ratio on the structural performance, additional hybrid analyses with

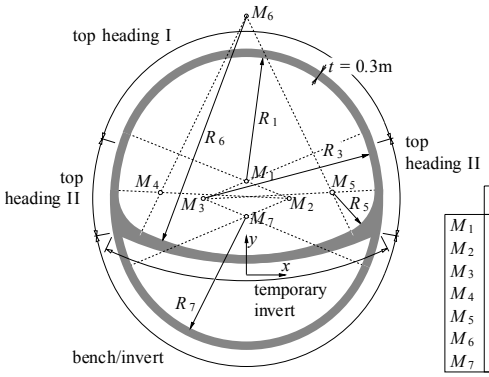

R_1	4.74
R_2	6.39
R_3	6.39
R_4	1.50
R_5	1.50
R_6	8.50
R_7	4.44

	x [m]	y [m]
M_1	0	3.40
M_2	1.52	2.77
M_3	-1.52	2.77
M_4	-3.06	3.00
M_5	3.06	3.00
M_6	0	9.30
M_7	0	2.14

Fig. 13 Lainzer tunnel: standard cross section (*M*: center point; *R*: radius).

intrinsic material functions determined for w/c=0.40 and w/c=0.60, respectively, were performed. The respective intrinsic material functions are given in **Fig. 14**.

Figure 15 shows the construction history for track 9 of the Lainzer tunnel. The reference time $t = 0$ is defined as the time instant characterizing the begin of construction work at the considered MCS, i.e., the excavation of the top heading I, which took place on January 23, 2001. 370 hours after the erection of top heading I, the excavation was interrupted for almost 69 days.

6.1 Thermochemical analysis

The hydration-kinetic model outlined in (Bernard *et al*. 2003; Pichler 2007) is used to determine the history of the hydration extents $\xi_x(t,r)$ and the temperature $T(t,r)$ in the lining, where τ represents the radial coordinate. Hereby, the different chemical reactions and their heat release are considered in the field equation of the underlying thermal problem, reading

$$\rho c\dot{T} - \sum_x l_{\xi_x}\dot{\xi}_x = -\operatorname{div}\mathbf{q} \tag{55}$$

where (ρc)[kJ/(K m^3)] denotes the volume heat capacity, and l_{ξ_x} [kJ/m^3] represents the heat release of the hydration reaction related to the x-th clinker phase in ordinary Portland cement. $\mathbf{q}$ [kJ/(m^2 h)] is the heat-flow vector. It is related to the temperature via Fourier's law of heat conduction:

$$\mathbf{q} = -k\,\operatorname{grad} T \tag{56}$$

where k [kJ/(m h)] denotes the thermal conductivity. At the inner surface of the lining, a radiation-type boundary condition is considered, with

$$\mathbf{q}\cdot\mathbf{n} = \alpha\left(T - T^{\infty}\right) \tag{57}$$

The employed material parameters used in the thermochemical analysis are summarized in **Table 1**. The output of the thermochemical analysis, i.e., the fields

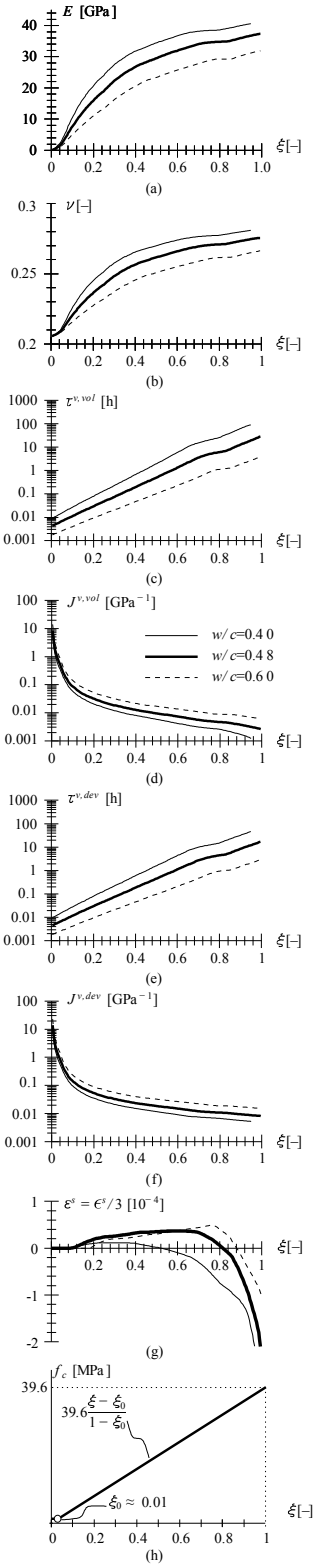

Fig. 14 Intrinsic material functions employed in hybrid analyses: (a) Young's modulus, (b) Poisson's ratio, (c) to (f) creep parameters obtained from multiscale model presented in this paper; (g) intrinsic material function for autogenous-shrinkage strains obtained from multiscale model reported in (Pichler et al. 2007; Pichler 2007), and (h) uniaxial strength obtained from macroscopic experiments.

Table 1 Material parameters and initial temperatures used in the thermochemical analysis.

		shotcrete	soil
Density ρ	[kg/m^3]	2400	1450
Heat capacity c	[kJ/(kg K)]	0.88	0.88
Thermal conductivity k	[kJ/(m h K)]	3.6	4.6
Radiation coefficient α_r	[kJ/(m^2 h K)]	40	-
Initial temperature T_0	[℃]	16	10
Temperature in tunnel opening T^∞	[℃]	18	-

$\xi(t,r)$ and $T(t,r)$, serve as input for the subsequent mechanical analysis of the considered MCS. The evolution of the temperature obtained at the center of the shotcrete lining shows a steep increase up to 65℃ within the first 12 hours, which agrees well with the temperature measurements performed at the construction site [see **Fig. 16(b)**]. Thereafter, the temperature approaches the stationary situation, which is reached within the first week after application of the lining. In contrast to previous publications dealing with thermochemical analyses of shotcrete linings (Pichler *et al*. 2003; Lackner and Mang 2002; Pichler and Lackner 2006), the *w*/*c*-ratio, which enters the hydration model affects the temperature increase in the lining. The higher the *w*/*c*-ratio, the more water is available for the hydration process, which results in an increased hydration rate (Bernard *et al*. 2003) and, thus, in a higher temperature rise in the lining.

6.2 Mechanical analysis

The temperature field and the fields of the reaction extents serve as input for the subsequent mechanical analysis. Hereby, the strain within each point of the lining is accessible via interpolation of displacement histories available at the aforementioned MPs. This strain field together with the actual temperature and reaction extents are considered in a multi-surface chemoplasticity model, accounting for stiffness growth, autogenous-shrinkage deformations, strength growth, microcracking, and creep (for details, see Lackner *et al*. (2002a); Lackner and Mang (2003)). For the interpretation of the numerical results obtained from the hybrid analysis of the considered MCS, the level of loading $\mathcal{L}$ is introduced. It amounts to 0% for the unloaded material and to 100% when the stress state reaches the failure surface defined by the (actual) compressive strength. For the underlying Drucker-Prager failure criterion, the level of loading at a point in the shotcrete lining is determined from Lackner and Mang (2003)

$$\mathcal{L} = \frac{\sqrt{J_2\left(\sigma_\varphi,\sigma_z\right)} + \alpha_{DP} I_1\left(\sigma_\varphi,\sigma_z\right)}{f_c\left(\xi\right)/\beta_{DP}} \tag{58}$$

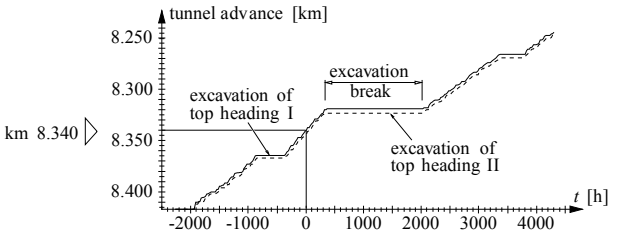

Fig. 15 Lainzer tunnel: construction history of tunnel containing track 9.

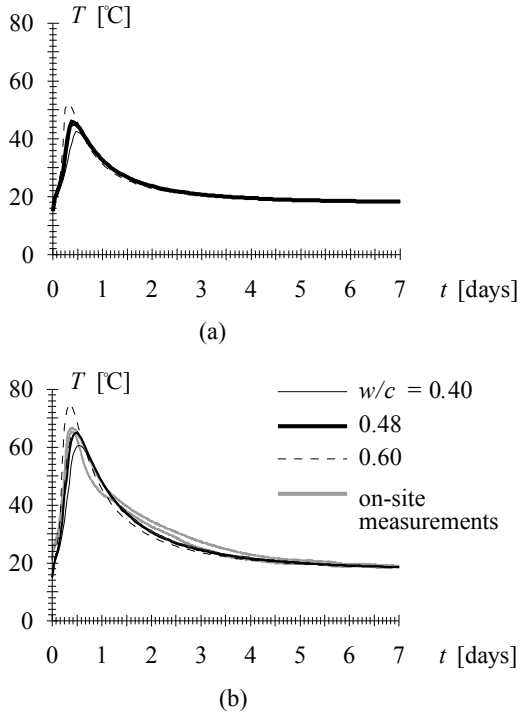

Fig. 16 Temperature history at (a) the inner surface and (b) the center of the lining.

where σ_φ and σ_z are the stress component in the circumferential and longitudinal direction of the tunnel. In Eq. (58), I_1 (J_2) represents the first (second) invariant of the stress tensor (deviator). α_{DP} and β_{DP} are constant parameters of the Drucker-Prager criterion, with $\alpha_{DP} = 0.699$ and $\beta_{DP} = 1.97$ (Lackner and Mang 2003). For presentation of the obtained results, the level of loading is averaged over the shell thickness h, with $\overline{\mathcal{L}} = \int_h \mathcal{L} dr$. **Figure 17** shows results from mechanical analyses with *w*/*c* = 0.48, when successively taking more and more dissipative phenomena into account. While **Fig. 17(b)** shows the result from an elastoplastic analysis disregarding autogenous shrinkage and creep, **Fig. 17(c)** is characterized by taking into account autogenous shrinkage. **Figure 17(b)** and **(c)** show only marginal differences. Hence autogenous deformations may be disregarded in the present analysis, characterized by *w*/*c* = 0.48[*11]. The increase of the level

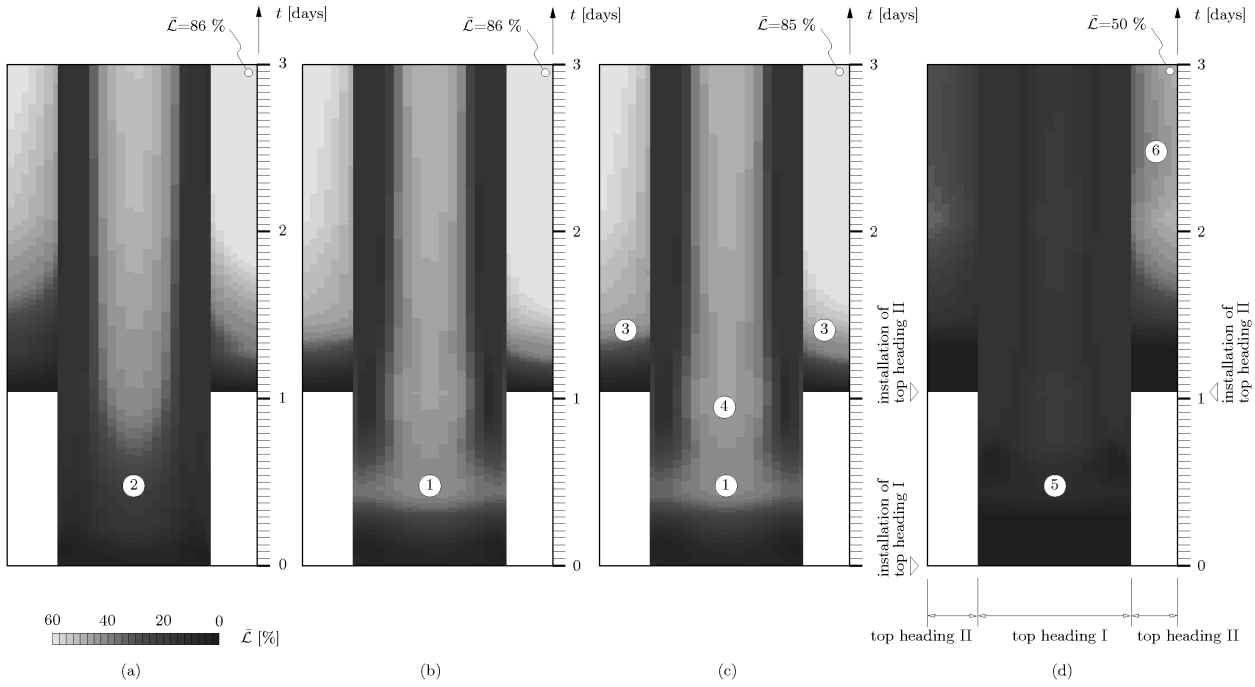

Fig. 17 History of distribution of $\bar{\mathcal{L}}$ in shotcrete lining (*w/c*=0.48) at considered MCS (top view of unrolled lining) for 3 days after application of top heading I: (a) elastoplastic analysis disregarding thermal dilation, (b) elastoplastic analysis, (c) elastoplastic analysis with autogenous shrinkage taken into account, and (d) viscoelastic-plastic analysis with autogenous shrinkage taken into account.

of loading within the first 12 hours [see ① in **Fig. 17(b)** and **(c)**]is caused by thermal dilation associated with the temperature rise in the course of the hydration process [compare to **Fig. 17(a)**, where thermal dilation was not taken into account, see ②], and the pronounced stiffness increase at early ages (see **Fig. 14**). This is observed for all newly-installed parts of the lining, i.e., top heading I and top heading II on both the left and the right side (see ③). Although the lining cools down after approximately 12 h (see **Fig. 16**), $\bar{\mathcal{L}}$ increases in the central part of top heading I (see ④). This is explained by the continuous excavation of top heading I and II, resulting in an increased loading of the lining by the inward-moving soil. When creep is taken into account [see **Fig. 18(d)**], the lining "dodges" excessive loading, particularly at early stages of hydration (see ⑤). Based on the measurements, and also reflected by the distribution of the level of loading, the MCS started to move towards the right bench, leading to a continuous, high loading of the right part of the lining (see ⑥). Consideration of creep deformations leads to a reduction of $\bar{\mathcal{L}}$ of approximately 36 % (compared to the elastoplastic analyses) in this part of the lining. **Fig. 18** shows the evolution of $\bar{\mathcal{L}}$ over the first 4.5 months. The surface settlements associated with the mentioned movement were the reason to stop the tunnel advance 370 hours after installation of the considered cross-section. During this construction break, the footings of the existing top heading II were improved by installing micropiles of 80 mm diameter.

In addition the aforementioned analyses, a parameter study was conducted in order to assess the influence of the *w/c*-ratio on the loading of the tunnel lining. The previous viscoelastic-plastic analysis characterized by consideration of autogenous shrinkage and *w/c* = 0.48 is compared to analyses for shotcrete with *w/c* = 0.40 and 0.60, respectively. Hereby, the employed intrinsic material functions, determined by the multiscale model, are given in **Fig. 14(a)** to **(g)**. The intrinsic material function for strength growth, on the other hand, given for shotcrete with *w/c* = 0.48 in **Fig. 14(h)**, remained unchanged in the present analyses. **Figure 19** compares the evolution of $\bar{\mathcal{L}}$ for the first 3 days. Whereas the increased stiffness for *w/c* = 0.40 leads to higher loading of the shotcrete lining, with $\bar{\mathcal{L}}$ =71 % at top heading II on the right side (t=3d), (i) the higher values for the elastic compliance and (ii) the significantly increased creep compliance for shotcrete characterized by *w/c* = 0.60 leads to a significant reduction of the level of loading to $\bar{\mathcal{L}}$ =9 %.

It is noteworthy, that for all analyses the same (measured) displacement histories at the considered MCS were

*[11] The smaller the *w/c* ratios, the larger are autogenous-shrinkage strains and, hence, the influence of the latter on structural performance, at early stages of hydration (Pichler et al. 2007).

used. Obviously, a different mix design of the employed shotcrete would have resulted in different displacements. However, because of the hybrid nature of the analysis, with displacement measurements from the construction site serving as input, the effect of the shotcrete mix on the displacement history cannot be considered.

7. Concluding remarks and future work

In this paper a multiscale model for early-age viscoelastic properties of cement-based materials was proposed and incorporated in the macroscopic analysis of shotcrete tunnel linings. Hereby, the viscous properties of the creep-active constituent at finer scales, i.e., calcium-silicate-hydrates are transferred to the macroscale,

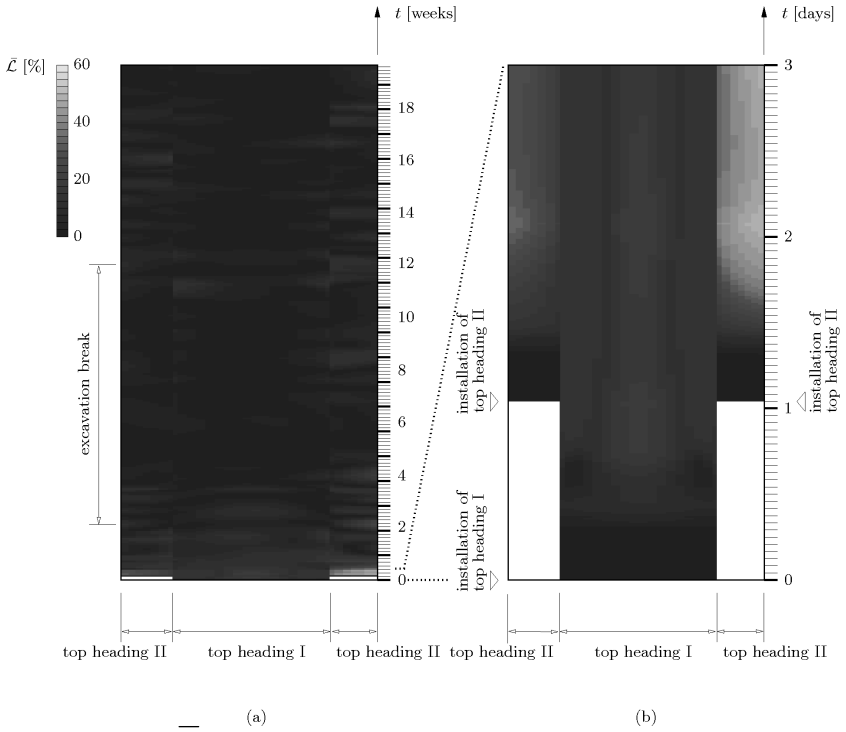

Fig. 18 History of distribution of $\overline{\mathcal{L}}$ in shotcrete lining (*w/c*=0.48) at considered MCS (top view of unrolled lining): (a) 4.5 months and (b) 3 days after application of top heading I.

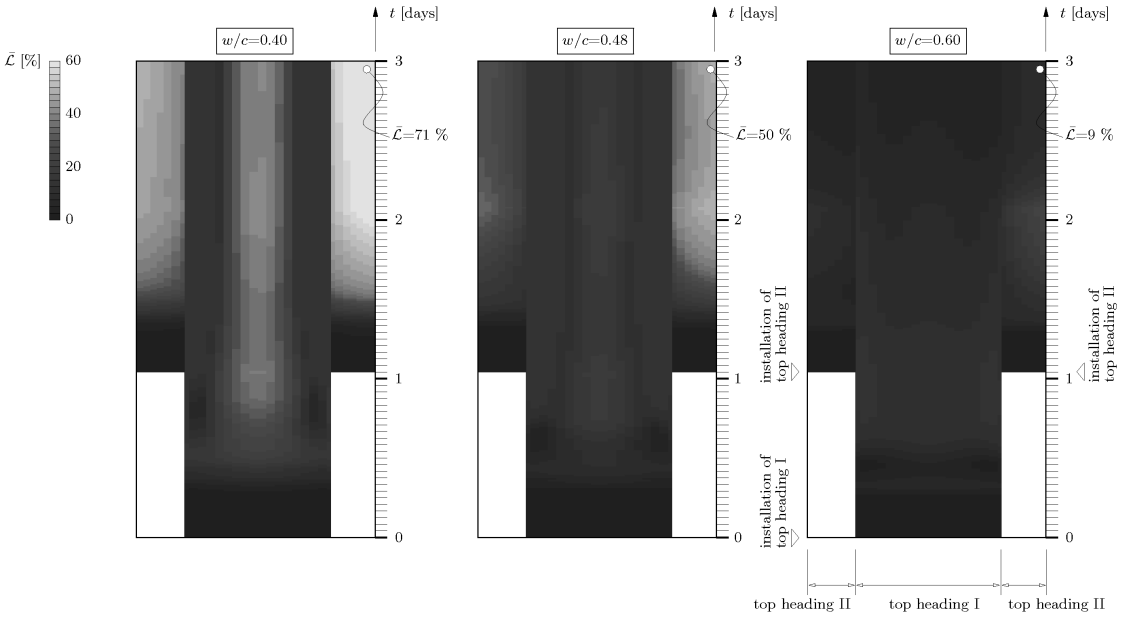

Fig. 19 History of distribution of $\overline{\mathcal{L}}$ in shotcrete lining at considered MCS (top view of unrolled lining) for 3 days after application of top heading I (parameter study for three different *w/c*-values).

considering the continuously changing finer-scale composition, as well as the compliance-raising effect of pores, and the stiffening effect of inclusion, respectively, at various observation scales.

The presented multiscale model may be improved by considering the influence of the curing temperature (other than T_0 =20 ℃) on the creep compliance parameter $J_{CSH}^{v,dev}$, accounting for the thermal activation of the creep process through an Arrhenius term, i.e., $J_{CSH}^{v,dev}$ (T_0)exp[E_a / R (1/ T − 1/ T_0)], with E_a denoting the activation energy of the long-term creep process (in Bažant (1995), the latter was identified as E_a / R =2700 K). Moreover, since magnitude and duration of the creep process was found to depend on the relative humidity h, the latter should also enter the evolution law for the degree of hydration ξ, particularly relevant for larger values of ξ. Both modes of improvement are topics of ongoing research.

Acknowledgment

Fruitful discussions on multiscale representation and modeling of concrete with Franz-Josef Ulm, Georgios Constantinides and Matthieu Vandamme during research stays of the first two authors at the MIT (Cambridge, MA) are gratefully acknowledged. Financial support granted by the Austrian Science Fund (FWF) via project P15912-N07 is appreciated.

References

Acker, P. and Ulm, F. -J. (2001). "Creep and shrinkage of concrete: physical origins and practical measurements." *Nuclear Engineering and Design*, 203, 148-158.

Athrushi, S. A. (2003). "Tensile and compressive creep of early age concrete: testing and modelling." Ph.D. thesis, The Norwegian University of Science and Technology, Trondheim, Norway.

Bažant, Z. P. (1979). "Thermodynamics of solidifying or melting viscoelastic material." *Journal of the Engineering Mechanics(ASCE)*, 105 (6), 933-952.

Bažant, Z. P. (1995). "Creep and damage in concrete." In: Skalnet, J., Mindess, S. (Eds.), *Materials Science of Concrete*. American Ceramic Society, Westerville, OH, pp. 335-389.

Bažant, Z. P., Hauggard, A., Baweja, S. and Ulm, F.-J. (1997). "Microprestress solidification theory for concrete creep, part I: Aging and drying effects." *Journal of Engineering Mechanics (ASCE)*, 123 (11), 1188-1194.

Bažant, Z. P. and Baweja, S. (1997). "Creep and shrinkage prediction model for analysis and design of concrete structures: model B3." In: Al-Maraseer (Ed.), SP-194: *The Adam Neville Symposium: Creep and Shrinkage-Structural Design Effects*. American Conrete Institue (ACI), Farmington Hills, MI, pp. 1-83.

Bentz, D. (1997). "Three-dimensional computer simulation of Portland cement hydration and microstructure development." *Journal of the American Ceramic Society*, 80 (1), 3-21, see also http://ciks.cbt.nist.gov/garbocz/AmCeram/.

Bernard, O., Ulm, F.-J. and Lemarchand, E. (2003). "A multiscale micromechanics-hydration model for the early-age elastic properties of cement-based materials." *Cement and Concrete Research*, 33, 1293-1309.

Beurthey, S. and Zaoui, A. (2000). "Structural morphology and relaxation spectra of viscoelastic heterogenous materials." *European Journal of Mechanics A / Solids*, 19, 1-16.

Cervera, M., Oliver, J. and Prato, T. (1999). "Thermo-chemo-mechanical model for concrete. II: damage and creep." *Journal of Engineering Mechanics (ASCE)*, 125 (9), 1028-1039.

Diamond, S. (2004). "The microstructure of cement paste and concrete－a visual primer." *Cement and Concrete Composites*, 26 (8), 919-933.

Eshelby, J. (1957). "The determination of the elastic field of an ellipsoidal inclusion, and related problems." *Proceedings of the Royal Society of London A*, 241, 376-396.

Hershey, A. (1954). "The elasticity of an isotropic aggregate of anisotropic cubic crystals." *Journal of Applied Mechanics (ASME)*, 21, 236-240.

Hummel, A., Wesche, K., Brand, W., Rüsch, H., Kordina, K. and Hilsdorf, H. (1962). "Versuche über das Kriechen unbewehrten Betons [Creep tests on plain concrete]." Tech. Rep. 146, Deutscher Ausschuß für Stahlbeton, Berlin, in German.

Jennings, H. M. (2000). "A model for the microstructure of calcium silicate hydrate in cement paste." *Cement and Concrete Research*, 30, 101-116.

Jennings, H. M. (2004). "Colloid model of C-S-H and implications to the problem of creep and shrinkage." *Materials and Structures*, 37, 59-70.

Kroener, E. (1958). "Berechnung der elastischen Konstanten des Vielkristalls aus den Konstanten des Einkristalls [Computation of the elastic constants of a polycrystal based on the constants of the single crystal]." *Zeitschrift für Physik*, 151, 504-518, in German.

Lackner, R., Hellmich, Ch. and Mang, H. A. (2002a). "Constitutive modeling of cementitious materials in the framework of chemoplasticity." *International Journal for Numerical Methods in Engineering*, 53 (10), 2357-2388.

Lackner, R., Macht, J. and Mang, H. A. (2002b). "Projekt zur Erstellung eines Programmsystems zur praktischen Umsetzung eines hybriden Verfahrens zur Bestimmung der Beanspruchung von Tunnelschalen aus Spritzbeton [Project for the development of a program system for the practical realization of a hybrid method for determination of the loading of shotcrete tunnel shells]." Tech. rep., Vienna University of Technology, Vienna, in German.

Lackner, R., Macht, J. and Mang, H. A. (2006). "Hybrid

analysis method for on-line quantification of stress states in tunnel shells." *Computer Methods in Applied Mechanics and Engineering*, 195 (41-43), 5361-5376.

Lackner, R. and Mang, H. A. (2002). "Modeling of early-age fracture of shotcrete: application to tunneling." In: Karihaloo, B. (Ed.), *Proceedings of the IUTAM Symposium on Analytical and Computational Fracture Mechanics of Nonhomogeneous Materials*. Kluwer Academic Publishers, Dordrecht, Cardiff, Wales, pp. 197-210.

Lackner, R. and Mang, H. (2003). "Cracking in shotcrete tunnel shells." *Engineering Fracture Mechanics*, 70, 1047-1068.

Laplante, P. (1993). "Propriétés mécaniques des bétons durcissants: analyse comparée des bétons classiques et à très hautes performances [Mechanical properties of hardening concrete: a comparative analysis of ordinary and high performance concretes]." Ph.D. thesis, Ecole Nationale des Ponts et Chaussées, Paris, France, in French.

Laws, N. and McLaughlin, R. (1978). "Self consistent estimates for the viscoelastic creep compliance of composite materials." *Proceedings of the Royal Society of London A*, 359, 251-273.

Lee, E. (1955). "Stress analysis in visco-elastic bodies." *Quarterly of Applied Mathematics*, 13, 183-190.

Mandel, J. (1966). "Mécanique des milieux continus [Continuum mechanics]." Gauthier, Paris, in French.

Mori, T. and Tanaka, K. (1973). "Average stress in matrix and average elastic energy of materials with misfitting inclusions." *Acta Metallurgica*, 21, 571-574.

Nabarro, F. (2001). "Creep mechanism in crystalline solids." *Encyclopedia of Materials: Science and Technology*, 1788-1795.

Neubauer, C. M. and Jennings, H. M. (2000). "The use of digital images to determine deformation throughout a microstructure. Part II: Application to cement paste." *Journal of Material Science*, 35, 5751-5765.

Pichler, Ch. (2007). "Multiscale characterization and modeling of creep and autogenous shrinkage of early-age cement-based materials." Ph.D. thesis, Vienna University of Technology.

Pichler, Ch., Lackner, R. and Mang, H. A. (2008). "Safety assessment of concrete tunnel linings under fire load." *Journal of Structural Engineering* (*ASCE*), 132 (6), 961-969.

Pichler, Ch. and Lackner, R. (2007). "Identification of logarithmic-type creep of calcium-silicate hydrates (CSH) by means of nanoindentation." *Strain*. In print.

Pichler, Ch., Lackner, R. and Mang, H. A. (2007). "A multiscale micromechanics model for the autogenous-shrinkage deformation of early-age cement-based materials." *Engineering Fracture Mechanics*, 74, 34-58.

Pichler, Ch., Lackner, R., Spira, Y. and Mang, H. A. (2003). "Thermochemomechanical assessment of ground improvement by jet grouting in tunneling." *Journal of Engineering Mechanics (ASCE)*, 129 (8), 951-962.

Ruetz, W. (1966). "Das Kriechen des Zementsteins im Beton und seine Beeinflussung durch gleichzeitiges Schwinden [Creep of cement in concrete and the influence of simultaneous shrinkage on this type of creep]." Deutscher Ausschuß für Stahlbeton , Heft 183, In German.

Sercombe, J., Hellmich, C., Ulm, F.-J. and Mang, H. A. (2000). "Modeling of early-age creep of shotcrete. I: model and model parameters." *Journal of Engineering Mechanics (ASCE)*, 126 (3), 284-291.

Simo, J. and Hughes, T. (1998). "Computational inelasticity." Springer, Berlin.

Stehfest, H. (1970). "Algorithm 368: Numerical inversion of Laplace transforms." *Communications of the ACM*, 13, 47-49.

Taylor, H. F. W. (1997). "Cement chemistry, 2nd Edition." Thomas Telford Publishing, London.

Tennis, P. D. and Jennings, H. M. (2000). "A model for two types of calcium silicate hydrate in the microstructure of portland cement pastes." *Cement and Concrete Research*, 30, 855-863.

Thomas, J. J. and Jennings, H. M. (2006). "A colloidal interpretation of chemical aging of C-S-H gel and and its effects on the properties of cement paste." *Cement and Concrete Research*, 36, 30-38.

Ulm, F.-J. (1998). "Couplages thermochémomécaniques dans les bétons : un premier bilan. [Thermochemomechanical couplings in concretes: a first review]." Tech. rep., Laboratoires des Ponts et Chaussées, Paris, France. In French.

Ulm, F.-J., Le Maou, F. and Boulay, C. (1999). "Creep and shrinkage couplings: new review of some evidence." *Revue Francaise de Génie Civil*. Ed. Hermès 3, 21-37.

Wittmann, F. (1982). "Creep and shrinkage mechanisms." In: Bažant, Z. P. and Wittmann, F. H. (Eds), *Creep and Shrinkage of Concrete Structures*, Wiley, Chichester, Ch. 6, 129-161.

Zaoui, A. (1997). "Structural morphology and constitutive behaviour of microheterogenous materials." In: Suquet, P. (Ed.), *Continuum micromechanics*. Springer, Vienna

Appendix 1. Algorithmic treatment

For the integration of the convolution integrals determining logarithmic creep in the context of a nonlinear FE-analysis, a discretized form of the state equation and the evolution equation for creep (and plasticity) is needed. Using a backward Euler scheme[*12], the discrete form of the evolution equation for the creep-strain tensor $\boldsymbol{\varepsilon}^v$ [see Eq.(43)] at the end of the (n+1)-st time increment, with $t_n \le t \le t_{n+1}$, follows from

$$\varepsilon^v_{n+1} = \sum_{k=1}^{n+1}\left\{\sum_{j=k}^{n+1}\Delta\mathbb{J}^{v,age}\left[t_j - t_k, \xi\left(t_j\right)\right]\right\} : \Delta\sigma_k \tag{A1}$$

and

$$\varepsilon^v_{n} = \sum_{k=1}^{n}\left\{\sum_{j=k}^{n}\Delta\mathbb{J}^{v,age}\left[t_j - t_k, \xi\left(t_j\right)\right]\right\} : \Delta\sigma_k \tag{A2}$$

with[*13]

$$\begin{aligned}&\Delta\mathbb{J}^{v,age}\left[t_j - t_k, \xi\left(t_j\right)\right] = \\ &\left\{\frac{1}{3}\mathbb{I}_{vol}\frac{J^{v,vol}_{eff}\left[\xi\left(t_j\right)\right]}{t_j - t_k + \tau^{v,vol}_{eff}\left[\xi\left(t_j\right)\right]} + \right. \\ &\left.\frac{1}{2}\mathbb{I}_{dev}\frac{J^{v,dev}_{eff}\left[\xi\left(t_j\right)\right]}{t_j - t_k + \tau^{v,dev}_{eff}\left[\xi\left(t_j\right)\right]}\right\}\left(t_j - t_{j-1}\right)\end{aligned} \tag{A4}$$

Hence, the increment of the creep-strain tensor is given as

$$\begin{aligned}&\Delta\varepsilon^v_{n+1} = \varepsilon^v_{n+1} - \varepsilon^v_n \\ &= \sum_{k=1}^{n}\left\{\sum_{j=k}^{n+1}\Delta\mathbb{J}^{v,age}\left[t_j - t_k, \xi\left(t_j\right)\right]\right\} : \Delta\boldsymbol{\sigma}_k + \\ &\quad \Delta\mathbb{J}^{v,age}\left[t_{n+1} - t_{n+1}, \xi\left(t_{n+1}\right)\right] : \Delta\boldsymbol{\sigma}_{n+1} - \\ &\quad \sum_{k=1}^{n}\left\{\sum_{j=k}^{n}\Delta\mathbb{J}^{v,age}\left[t_j - t_k, \xi\left(t_j\right)\right]\right\} : \Delta\boldsymbol{\sigma}_k \\ &= \sum_{k=1}^{n}\left\{\sum_{j=k}^{n+1}\Delta\mathbb{J}^{v,age}\left[t_j - t_k, \xi\left(t_j\right)\right] - \right. \\ &\quad \left.\sum_{j=k}^{n}\Delta\mathbb{J}^{v,age}\left[t_j - t_k, \xi\left(t_j\right)\right]\right\} : \Delta\boldsymbol{\sigma}_k + \\ &\quad \Delta\mathbb{J}^{v,age}\left[t_{n+1} - t_{n+1}, \xi\left(t_{n+1}\right)\right] : \Delta\boldsymbol{\sigma}_{n+1} \\ &= \sum_{k=1}^{n}\Delta\mathbb{J}^{v,age}\left[t_{n+1} - t_k, \xi\left(t_{n+1}\right)\right] : \Delta\boldsymbol{\sigma}_k + \\ &\quad \Delta\mathbb{J}^{v,age}\left[t_{n+1} - t_{n+1}, \xi\left(t_{n+1}\right)\right] : \Delta\boldsymbol{\sigma}_{n+1}\end{aligned} \tag{A5}$$

Accounting for the stress-free formation of hydration products (Bažant 1979), a differential form of the state equation is employed (Lackner *et al*. 2002a). Writing the state equation in discretized form one gets

$$\Delta\boldsymbol{\sigma}_{n+1} = \mathbb{C}\left(\xi_{n+1}\right) : \left[\Delta\boldsymbol{\varepsilon}_{n+1} - \Delta\boldsymbol{\varepsilon}^p_{n+1} - \Delta\boldsymbol{\varepsilon}^v_{n+1}\right] \tag{A6}$$

Reformulating Eq. (A6) in order to obtain the standard plasticity format gives[*14]

$$\begin{aligned}\Delta\boldsymbol{\sigma}_{n+1} = \mathbb{C}\left(\xi_{n+1}\right) : \{&\Delta\boldsymbol{\varepsilon}_{n+1} - \Delta\boldsymbol{\varepsilon}^p_{n+1} - \\ &\sum_{k=1}^{n}\Delta\mathbb{J}^{v,age}\left[t_{n+1} - t_k, \xi\left(t_{n+1}\right)\right] : \Delta\boldsymbol{\sigma}_k - \\ &\Delta\mathbb{J}^{v,age}\left[t_{n+1} - t_{n+1}, \xi\left(t_{n+1}\right)\right] : \Delta\boldsymbol{\sigma}_{n+1}\}\end{aligned} \tag{A7}$$

and

$$\begin{aligned}&\left\{\mathbb{I} + \mathbb{C}\left(\xi_{n+1}\right) : \Delta\mathbb{J}^{v,age}\left[t_{n+1} - t_{n+1}, \xi\left(t_{n+1}\right)\right]\right\} : \Delta\boldsymbol{\sigma}_{n+1} \\ &= \mathbb{C}\left(\xi_{n+1}\right) : \{\Delta\boldsymbol{\varepsilon}_{n+1} - \Delta\boldsymbol{\varepsilon}^p_{n+1} - \\ &\quad \sum_{k=1}^{n}\Delta\mathbb{J}^{v,age}\left[t_{n+1} - t_k, \xi\left(t_{n+1}\right)\right] : \Delta\boldsymbol{\sigma}_k\}\end{aligned} \tag{A8}$$

and, finally,

$$\begin{aligned}&\Delta\boldsymbol{\sigma}_{n+1} = \\ &\left\{\mathbb{I} + \mathbb{C}\left(\xi_{n+1}\right) : \Delta\mathbb{J}^{v,age}\left[t_{n+1} - t_{n+1}, \xi\left(t_{n+1}\right)\right]\right\}^{-1} : \\ &\mathbb{C}\left(\xi_{n+1}\right) : \{\Delta\boldsymbol{\varepsilon}_{n+1} - \Delta\boldsymbol{\varepsilon}^p_{n+1} - \\ &\quad \sum_{k=1}^{n}\Delta\mathbb{J}^{v,age}\left[t_{n+1} - t_k, \xi\left(t_{n+1}\right)\right] : \Delta\boldsymbol{\sigma}_k\}\end{aligned} \tag{A9}$$

where $\mathbb{I}$ represents the fourth-order unity tensor. Thus, the standard format of elastoplasticity is obtained, where only $\Delta\boldsymbol{\varepsilon}^p_{n+1}$ depends on the unknown stress tensor. For the solution of Eq. (A9), return map algorithms as outlined in Simo and Hughes (1998) are used.

[*12] An implicit integration scheme is used in this work, i.e., quantities changing in time are assumed as constant in the time interval $[t_n, t_{n+1}]$, taking their value at the end of the time interval.

[*13] In Eq. (A4), the stress increment $\Delta\boldsymbol{\sigma}_k$ is assumed to be applied at the end of the respective time increment. If the stress increment is applied at the beginning of the respective time increment, Eq. (A4) reads

$$\begin{aligned}&\Delta\mathbb{J}^{v,age}[t_j - t_{k-\alpha}, \xi(t_j)] = \\ &\left\{\frac{1}{3}\mathbb{I}_{vol}\frac{J^{v,vol}_{eff}[\xi(t_j)]}{t_j - t_{k-\alpha} + \tau^{v,vol}_{eff}[\xi(t_j)]} + \right. \\ &\left.\frac{1}{2}\mathbb{I}_{dev}\frac{J^{v,dev}_{eff}[\xi(t_j)]}{t_j - t_{k-\alpha} + \tau^{v,dev}_{eff}[\xi(t_j)]}\right\}(t_j - t_{j-1})\end{aligned} \tag{A3}$$

with α =1. In case the stress increment is applied in the a middle of the time increment, α =1/2.

[*14] In Eq. (A6) both the plastic strain increment $\Delta\boldsymbol{\varepsilon}^p_{n+1}$ and the viscous strain increment $\Delta\boldsymbol{\varepsilon}^v_{n+1}$ depend on $\Delta\sigma_{n+1}$. On the right-hand-side of the respective law for classical elastoplasticity only $\Delta\boldsymbol{\varepsilon}^p_{n+1}$ depends on $\Delta\boldsymbol{\sigma}_{n+1}$. In order to obtain the same mode of dependence as in classical elastoplasticity, Eq. (A6) is reformulated.

Appendix 2. Input-parameter sets for multiscale model

This appendix summarizes input-parameter sets, characterizing various cement-based materials used to verify the multiscale model. The input parameters include the basic mix properties (water/cement-ratio *w*/*c* and cement content c), the elastic properties of the aggregate, as well as parameters characterizing the employed cement (Blaine fineness ø, medium initial radius of the clinker grains *R*, and the mass fractions of the clinker phases). Mineralogical analyses of OPC clinker give access to the mass fractions of lime CaO, silica SiO_2, alumina Al_2O_3, ferrite Fe_2O_3, sulphate SO_3, ... The mass fractions of the clinker phases are determined by the so-called Bogue calculation (Taylor 1997). For this calculation, the lime content m_{CaO} is reduced by the content bound in gypsum $CaSO_4 \cdot H_2O$ (written in abbreviated form $C\bar{S}H_2$), with 1 mol SO_3 combining with 1 mol CaO to form gypsum or, equivalently, 80 g SO_3 binding 56 g CaO. Hence, the mass fraction of sulphate m_{SO_3} combines with 56/80 m_{SO_3} of CaO. Other parameters, when required for verification of the model, e.g., the compressive strength and the aggregate/cement ratio *a*/*c* for comparison of the modeled creep compliance with the B3 model (Bažant and Baweja 1997) are also listed in the tables.

Appendix 2(a) Input-parameter set for multiscale model for the shotcrete employed at the Lainzer tunnel.

Basic mix properties:		
Water/cement-ratio *w/c*	[–]	0.48
Cement content *c*	[kg/m^3]	380
Elastic properties of aggregate:		
Young's modulus of aggregate E_a	[GPa]	50
Poisson's ratio of aggregate v_a	[–]	0.3
Cement characteristics:		
Blaine fineness ø	[cm^2/g]	4895
Medium initial radius of clinker grains *R*	[μm]	5
Mass fractions of clinker phases		
m_{C_3S}	[%]	48.7
m_{C_2S}	[%]	22.8
m_{C_3A}	[%]	11.4
m_{C_4AF}	[%]	9.4
$m_{C\bar{S}H_2}$	[%]	7.7
Additional parameters for model verification:		
Curing temperature *T* (isothermal conditions)	[°C]	11
Experiments conducted on specimens of age ...	[h] [d]	2;4;8;12 1;2;7;28
Aggregate/cement-ratio *a*/*c*[1]	[–]	5.3
Compressive strength $f_{c\infty}$ [1]	[MPa]	40.0

[1] parameters for comparison with B3 model (Bažant and Baweja 1997)

Appendix 2(b) Input-parameter set for multiscale model (upscaling of creep properties) for concrete investigated in Laplante (1993).

Creep experiments published in ...		Laplante (1993)	
Type of concrete (notation in reference)		BO	BTHP
Basic mix properties:			
Water/cement-ratio *w/c*	[–]	0.50	0.33
Cement content *c*	[kg/m^3]	342	398
Elastic properties of aggregate:			
Young's modulus of aggregate E_a	[GPa]	65	65
Poisson's ratio of aggregate v_a	[–]	0.23	0.23
Cement characteristics:			
Blaine fineness ø	[cm^2/g]	3466	3466
Medium initial radius of clinker grains *R*	[μm]	(8)	(8)
Mass fractions of clinker phases			
m_{C_3S}	[%]	60.7	60.7
m_{C_2S}	[%]	18.7	18.7
m_{C_3A}	[%]	2.8	2.8
m_{C_4AF}	[%]	12.2	12.2
$m_{C\bar{S}H_2}$	[%]	2.5	2.5
others+inert	[%]	3.1	3.1
Additional parameters for model verification:			
Curing temperature *T* (isothermal conditions)	[°C]	20	20
Loading times t_0	[h]	20; 27	20;24; 28
	[d]	3;7; 28	3;7; 28
Aggregate/cement-ratio *a*/*c*[1]	[–]	5.46	4.84
Compressive strength f_{c28} [1]	[MPa]	40	80

[1] parameters for comparison with B3 model (Bažant and Baweja 1997)

Appendix 2(c) Input-parameter set for multiscale model (upscaling of creep properties) for concrete investigated in Hummel *et al*. (1962).

Creep experiments published in ...		Hummel *et al*. (1962)					Athrushi (2003)	
Type of cement (notation in reference)		PZ 225	PZ 225	PZ 225	PZ 225	PZ 425	BASE5	Maridal
Basic mix properties:								
Water/cement-ratio *w/c*	[–]	0.38	0.45	0.55	0.65	0.55	0.42	0.44
Cement content *c*	[kg/m^3]	350	345	334	328	334	368.1	350
Elastic properties of aggregate:								
Young's modulus of aggregate[1] E_a	[GPa]	(40)	(40)	(40)	(40)	(40)	(40)[4]	(50)[4]
Poisson's ratio of aggregate v_a	[–]	(0.3)	(0.3)	(0.3)	(0.3)	(0.3)	(0.3)	(0.3)
Cement characteristics:								
Blaine fineness ø	[cm^2/g]	3900	3900	3900	3900	4575	3600[5]	3600[5]
Medium initial radius of clinker grains *R*	[μm]	(7)	(7)	(7)	(7)	(5)	(8)	(8)
Mass fractions of clinker phases[2]								
m_{C_3S}	[%]	49.1	49.1	49.1	49.1	53.6	(55)	(55)
m_{C_2S}	[%]	23.0	23.0	23.0	23.0	13.2	(23)	(23)
m_{C_3A}	[%]	8.0	8.0	8.0	8.0	10.7	6,0	6.0
m_{C_4AF}	[%]	7.6	7.6	7.6	7.6	9.6	(6.2)	(6.2)
$m_{C\bar{S}H_2}$	[%]	3.7	3.7	3.7	3.7	4.7	4.8	4.8
Others+inert	[%]	8.6	8.6	8.6	8.6	8.2	(5)	(5)
Additional parameters for model verification:								
Curing temperature (isothermal conditions)	[℃]	20	20	20	20	20	20	20
Loading times t_0	[d]	28	28	3;28;90	28	3;28;90	1;2;3; 4;6;8	2;3;6
Aggregate/cement-ratio *a/c*[3]	[–]	5.4	5.4	5.4	5.4	5.4	5.12	5.24
Compressive strength f_{c28}[3]	[MPa]	41.4	34.9	28.6	20.3	43.5	81.0	42.2

[1] Rhine gravel,
[2] 4% ignition loss was taken into account
[3] parameters for comparison with B3 model (Bažant and Baweja 1997) (cylinder 15/30 cm)
[4] chosen to match macroscopic stiffness evolution (E_{28})
[5] Norcem Anleggsement CEM I 52.5 N-LA, data taken from www.norcem.org